Università degli Studi di Padova

Dipartimento di Ingegneria Industriale
Corso di Laurea Magistrale in Ingegneria Aerospaziale

Tesi di Laurea Magistrale

CFD Study of an Installed Transonic Rotor

Laureanda:
Elisa Fior

Relatore:
Prof. Ernesto Benini

Correlatore:
Ing. Andrea Magrini

Anno accademico 2018 / 2019

Alla mia famiglia
ai miei amici
a tutti coloro che mi hanno sostenuta durante questo percorso

Nomenclature

$UHBPR$	Ultra High Bypass Ratio
B, BPR	Bypass Ratio
CA, HA	Cold Airflow, Hot Airflow
$TSFC$	Thrust Specific Fuel Consumption
FPR	Fan Pressure Ratio
CFD	Computational Fluid Dynamics
NS, N, NE	Nacelle Sting, Isolated Nacelle, Nacelle with Exhaust
CRM	Common Research Model
NPF	Net Propulsive Force
TFN	Through Flow Nacelle
$WBNP$	Wing Body Nacelle Pylon
WB	Wing Body (clean wing)
$AoA_{A/C}$	Angle of Attack for an Aircraft Axis
GPF	Gross Propulsive Force
GPF_{ξ}	Gross Propulsive Force in Engine Axis Direction
dc	Drag Count
ADP	Aerodynamic Design Point
T/O	Take-Off
LE	Leading Edge
TE	Trailing Edge
IGV	Inlet Guide Vanes
OGV	Outlet Guide Vanes
RPM	Revolutions Per Minute
ATM	Automatic Topology and Meshing
$R67$	Rotor 67
SST	Shear Stress Transport
BC	Boundary Conditions
$\dot{m}$ $[kg/s]$	Mass Flow Rate
$\dot{m}_{TOT}$ $[kg/s]$	Total Inlet Mass Flow Rate
R $[N]$	Thrust
R_s $[Ns/kg]$	Specific Thrust
c, V $[m/s]$	Velocity
c_e, c_a $[m/s]$	Exhaust Velocity, Flight Velocity
AoA, α $[deg]$	Angle of Attack, Incidence Angle
$\eta_{P,is}$ $[-]$	Propulsive and Isentropic Efficiency
M $[-]$	Mach Number
$M_{\infty,cr,DR}$ $[-]$	Freestream, Critical, Drag Rise Mach Number
c_D $[-]$	Drag Coefficient
A $[m^2]$	Area
A_i $[m^2]$	Highlight Area

A_∞ $[m^2]$	Streamtube Capture Area
A_m $[m^2]$	Maximum Nacelle Area
D $[N]$	Drag
V_∞ $[m/s]$	Freestream Velocity
p $[Pa]$	Static Pressure
n $[-]$	Unit Normal
τ $[Pa]$	Shear Stress
$[x, y, z]$ $[-]$	Cartesian Coordinates
D' $[N]$	Modified Drag
$c_{D'}$ $[-]$	Modified Drag Coefficient
c_f $[-]$	Skin Friction Coefficient
$A_{wc,ws}$ $[m^2]$	Wetted Cowl and Wetted Sting Area
$c_{D,spill}$ $[-]$	Spillage Drag Coefficient
c_p $[-]$	Pressure Coefficient
c $[m]$	Chord
c_L $[-]$	Lift Coefficient
$\Delta c_{D,inst}$ $[-]$	Installation Drag
L $[m]$	Inlet Length
D $[m]$	Diameter
η_{pol} $[-]$	Polytropic Efficiency
L, L_{is} $[J/kg]$	Work, Isentropic Work
T^0 $[K]$	Total Temperature
h^0 $[J/kg]$	Total Enthalpy
π_c $[-]$	Total Pressure Ratio
$\dot{m}_c$ $[kg/s]$	Corrected Mass Flow Rate
N_c $[RPM]$	Corrected Rotational Speed
$u*$ $[m/s]$	Friction Velocity
Δs $[m]$	Initial Wall Sopacing
ν $[m^2/s]$	Kinematic Viscosity
w $[m/s]$	Relative Velocity
u $[m/s]$	Tangential Blade Speed
r $[m]$	Radius
$A*, A_{FF}$ $[m^2]$	Critical and Fan Face Area
$r_{i,FF}$ $[m]$	Highlight and Fan Face Radius
a $[m/s]$	Local Speed of Sound
T $[K]$	Static Temperature
R $[J/(kgK)]$	Gas Constant
$c_{P,v}$ $[J/(kgK)]$	Specific Heat at Constant Pressure/Volume
η_D $[-]$	Isentropic Diffusion Efficiency
π_D $[-]$	Intake's Total Pressure Loss
T_{amb} $[K]$	Static Temperature at Ambient Condition
p_{amb} $[Pa]$	Static Pressure at Ambient Condition

Contents

List of Figures

List of Tables

Sommario

Nel campo dell'aviazione civile, la riduzione dei consumi e dell'inquinamento prodotto dai motori aeronautici, rappresenta, ad oggi, l'obiettivo di maggior rilevanza.
L'ottenimento di propulsori sempre meno inquinanti passa attraverso un progressivo aumento dell'efficienza propulsiva, nonché un calo della resistenza aerodinamica, target conseguibili con l'adozione di nuove tecniche, tra le quali l'introduzione di motori turbofan ad alto rapporto di bypass e l'utilizzo di nacelles corte, configurazioni che prevedono l'utilizzo di fan a basso rapporto di compressione.
Tuttavia, l'installazione del motore rappresenta da sempre una sfida per i progettisti, in quanto le prestazioni del propulsore e, più in generale, dell'intero velivolo, vengono notevolmente influenzate dalla presenza della nacelle, la quale si stima che produca circa il 61% della totale resistenza aerodinamica [2]. Si deve perciò cercare di ridurre, per quanto possibile, questo valore.
Nella realtà, ancor prima di questo, il primo aspetto a cui prestare attenzione è la corretta installazione del fan all'interno della presa dinamica, poiché il mal posizionamento di quest'ultimo influenzerebbe sensibilmente le prestazioni globali della macchina.
Nel corso del presente lavoro viene studiata, tramite delle simulazioni CFD, l'interazione tra un fan transonico, il Nasa rotor 67, ed una nacelle con presa dinamica di lunghezza tradizionale [4] al fine di constatare se tale accoppiamento possa rappresentare una configurazione realistica sulla quale porre le basi per future analisi che prevedano una presa dinamica di lunghezza ridotta. A questo proposito, i criteri di verifica si basano sull'analisi della forma del tubo di flusso in ingresso al propulsore per due diverse condizioni di flusso indisturbato, sulle prestazioni del rotore in termini di mappe caratteristiche ed evoluzione del numero di Mach, ed infine sull'analisi delle prestazioni della presa dinamica.
I risultati ottenuti confermano la corretta installazione del fan all'interno della nacelle, il cui posizionamento è da ritenersi di primaria importanza, stando perciò alla base dell'intero processo di costruzione della mesh.

Abstract

Currently, one of the most relevant goals for civil aviation is the reduction of fuel consumption and pollution from aeronautical engines.
To obtain propulsors which are more environmentally friendly, there needs to be a gradual increase in propulsive efficiency, as well as a decrease in terms of drag force. This target is achievable through the use of new techniques, such as ultra high bypass ratio turbofan engines and short nacelle as these feature a low fan pressure ratio configuration.
However, the engine installation has always represented a challenge for designers due to propulsor performances and, more generally, those of the aircraft as a whole. Performance is considerably influenced by nacelle's installation, which is estimated to produce about 61% of the whole drag [2]. Knowing this, it is unquestionably necessary to try and reduce this value as much as possible. Prior to this, however, it is important to ensure the correct installation of the fan within the intake as a misplacement would have a significant influence on the machine's global performance.
In the present work, the interaction between a transonic fan, the Nasa rotor 67, and a nacelle with a traditional intake's length [4], is examined by means of CFD simulations, so as to evaluate whether this match may represent a realistic configuration on which to model future analysis, featuring a shorter intake. In this regard, checking criteria are based on the shape of pre-entry streamtube's analysis for two different undisturbed stream conditions; on rotor's performances in terms of characteristic maps and evolution of Mach number; and on the analysis of intake's performances.
The obtained results confirm that the fan's installation inside the nacelle is correct, the placement of which is of significant importance as it acts as the foundation of the entire mesh generation process.

- I -

Introduction and Literature Review

Currently, one of the most important targets of civil aviation is to improve aircrafts' efficiency, especially through a substantial reduction of fuel burn. This alteration would ultimately decrease not only the environmental impact, but also the costs to consumers.
To achieve this objective, the aviation industry is now studying some new propulsion technologies for future aircrafts, focusing firstly on airplane drag as the overall efficiency increases by improving drag reduction. Undeniably, to meet improvement of overall efficiency targets, it is foremost important to ensure the correct installation and integration of the engine with the airframe [3].
To increase propulsive efficiency, the improvement in engine technologies is focused to the development of UHBPR (ultra high bypass ratio) turbofan engines. Consequently though the engine diameter tends to substantially grow, with an increasing nacelle drag and weight, offsetting some of the achieved benefits coming from the use of UHBPR engines. Current values of BPR are close to 11, but it is expected that for future configurations this parameter will reach values closer to 15+ at design point.

The aim of this work is a CFD study of the interaction between a fan blade, a nacelle and a spinner. The considered fan consists on the Rotor 67 transonic blade provided by Nasa, which is inserted in a nacelle extracted from the Nasa CRM, while the spinner geometry is built using Solidworks and then coupled with the other two components in order to obtain a single channel simulation.
Before considering the complete model, the validation is made on the single passage blade without considering spinner and nacelle components.
Once the validation is completed, the work proceeds with the construction of the entire model mesh. Since nacelle, blade and spinner are not designed to work together, it is necessary to pay attention on their relative positions to verify the correct installation. This last step is carried out with a Matlab code, written specifically to provide the right axial location where to position the fan face on nacelle's axis in order to properly simulate a realistic case.
Obtained results are examined in terms of streamtubes and fan characteristic maps are compared with those achieved from validation analysis, moreover aerodynamic problems related to the functioning under variable conditions are investigated.

This thesis wants to lay the foundations for future works based on installation effects and drag assessment, in particular how these vary and influence engine's performances consequently to short nacelles adoption during a wide range of flight conditions, such as take-off, climb, cruise, crosswind and landing. This requirement of investigation about new intake configurations arises from the will as well as the need to make aircraft's engines even more environmental friendly by means of UHBPR turbofans, transonic fans and shorter inlets to improve drag effects and fuel burn reduction; so the work aims to give a starting point for future aerodynamic analysis and an overall view of the interaction among the Nasa rotor 67 transonic fan and a traditional intake.
To summarize the thesis' structure, the first chapter aims to give an overview of the main installation aspects, ultra-short nacelles for future engine's configurations and some information about turbomachinery are given. The next one presents the validation process and its results so as to confirm the validity of the CFD model, entire model mesh construction and case setup are illustrated too.
The last chapter presents and discusses the obtained results.

1.1 Aero-engine Installation

As previously mentioned, when considering future airplane propulsors, it is necessary to focus on installation and integration of the engine. This is especially true at cruise condition, as it is the most dominant phase during flight. The increase in bypass ratio of turbofan engines leads to larger fans, which in turn means larger nacelles, and consequently the augmentation of their drag contribute.

Firstly, some aspects of turbofan engines have to be explained.
A turbofan is an airbreathing jet engine largely used especially in civil aviation; it consists of a turbojet with the addition of a fan right upstream the compressor. In this way, the incoming airflow which passes through the fan will be then divided into two parts: one is processed by the turbojet (called hot airflow) and the other (called cold airflow) instead passes through the bypass duct and it is not subjected to thermodynamic transformations.

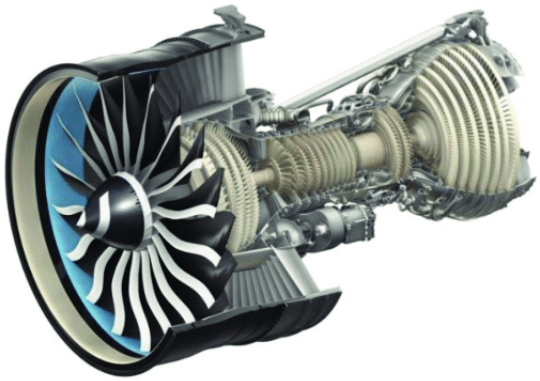

Figure 1.1: *An example of turbofan engine.*

For turbofan engines the ratio between the cold airflow and the hot one is defined as *Bypass ratio*:

$$B = \frac{\dot{m}_{CA}}{\dot{m}_{HA}} \tag{1.1}$$

Differently from turbojet engines, the adoption of turbofans allows an increase of propulsive efficiency because of the decrease of exhaust velocity. As a portion of the turbine's energy is used to move the fan, the specific thrust is reduced and the ingested airflow increases with the effect of less exhaust velocity therefore higher propulsive efficiency [1]. These aspects can be seen also referring to Equation 1.2, 1.3:

$$R_s = \frac{R}{\dot{m}_{TOT}} = (1+f)c_e - c_a \tag{1.2}$$

$$\eta_P = \frac{Rc_a}{\dot{m}_{TOT}[(1+f)c_e^2/2 - c_a^2/2]} \tag{1.3}$$

- R_s is the specific thrust
- R is the thrust
- $\dot{m}_{TOT}$ is the total mass flow rate entering the propulsor
- f is defined as $\frac{\dot{m}_{fuel}}{\dot{m}_{CA}}$
- c_e and c_a are the exhaust velocity and flight velocity respectively
- η_P is the propulsive efficiency

From last equations it can be seen that, assuming thrust as constant, increasing the incoming mass flow leads to less specific thrust and lower R_s values mean also lower c_e. To better understand the link between specific thrust and propulsive efficiency, it is useful to consider thrust equation:

$$R = \dot{m}[(1+f)c_e - c_a] \tag{1.4}$$

Since f«1 and combining Equation 1.4 with 1.3, propulsive efficiency as a function of specific thrust is obtained:

$$\eta_P = \frac{2}{2 + \frac{R_s}{c_a}} \tag{1.5}$$

Figure 1.2 is a graphical representation of the above equation.

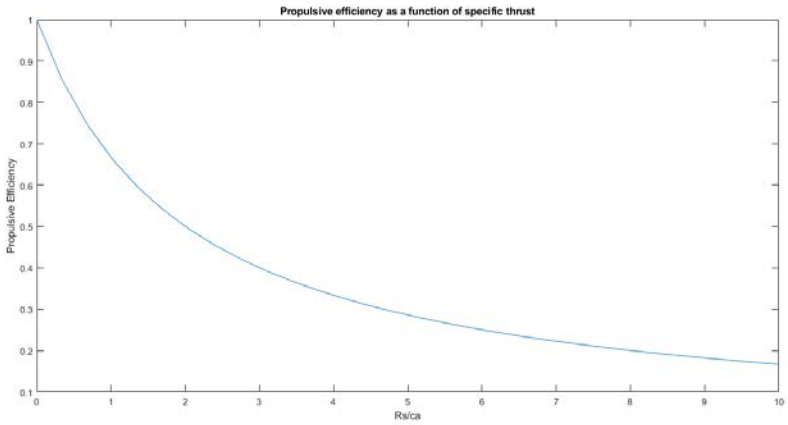

Figure 1.2: *Propulsive efficiency function of R_s/c_a.*

If c_a is considered constant, the previous figure highlights how is not possible to obtain both high specific thrust and propulsive efficiency, therefore engines which develop high η_P values are generally very large with high inlet mass flow rate and small specific thrust values.

Since the trend with future turbofans is to increase bypass ratio, it is of fundamental importance to analyse how specific thrust, TSFC (Thrust Specific Fuel Consumption), propulsive efficiency and FPR (Fan Pressure Ratio) change as BPR increases.

Figure 1.3 shows better performances in terms of TSFC and propulsive efficiency as the bypass ratio increases: TSFC is linked to environmental impact and higher values of

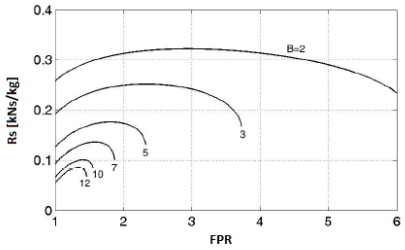

(a) *Specific thrust as a function of FPR.*

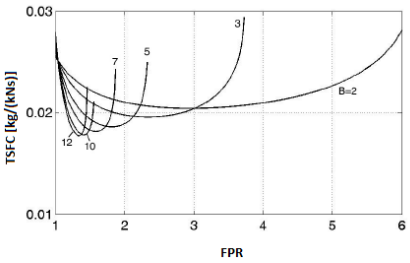

(b) *TSFC as a function of FPR.*

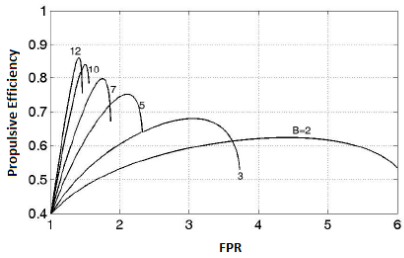

(c) *Propulsive efficiency as a function of FPR.*

Figure 1.3: *Bypass ratio influence on turbofan performance parameters [1].*

BPR lead to fuel saving. However, from all previous plots an FPR reduction comes to light when BPR grows, therefore the adoption of UHBPR engines causes lower FPR values for next turbofan generations.

1.1.1 Drag evaluation

According to [10], [2], the nacelle produces a huge part of an aircraft's total drag, therefore its design is of fundamental importance, especially considering future larger UHBPR engines. Several studies were carried out to predict drag influence on nacelle's performance using wind tunnel and CFD.
Generally, the drag for an aircraft flying at transonic speed can be separated into three components [11]:

1. Viscous drag
2. Induced drag
3. Wave drag

In a nacelle exposed to transonic airflow, even though flight velocity could be smaller than speed of sound, there will be at least a portion on the nacelle's external surface in which the Mach number exceeds unity. This region of supersonic flow normally ends with a shock wave which contributes to increasing overall drag; known as the *wave drag*. This phenomenon increases as the freestream Mach number increases. Below, a detailed explanation of this kind of drag is provided.
The value of M_∞ (freestream Mach number) which allows the comparison of the first sonic point on the surface is called *critical Mach number*. As M_∞ increases, this sonic point becomes a sonic line which divides the supersonic region (near body surface) from the subsonic one with the creation of a shock wave.
Focusing on drag coefficient, when M_∞ exceeds M_{cr}, it starts increasing until freestream Mach number reaches the *drag rise Mach number* (M_{DR}). At this point, c_D spikes rapidly.

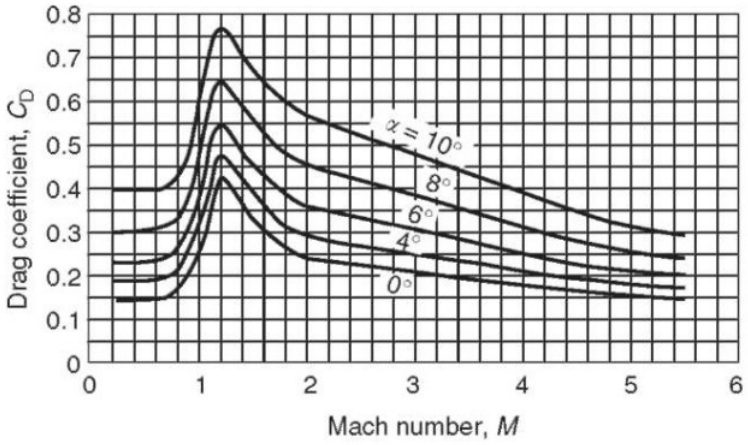

Figure 1.4: *Drag coefficient variations vs. Mach number at some AoA α.*

From Figure 1.4, instinctively, it is possible to affirm that, the higher M_{DR} is, the bigger the delay in drag's rapid increase. Therefore it is important to define the right geometry which is able to guarantee the highest M_{DR} value.

Some definitions of M_{DR} can be found in literature, even though they're not properly defined for nacelles but for the full aircraft drag rise [2]. Drag assessment study conducted in [2] refers to the following explanation given by Roskam [12]:

$$\left.\frac{\partial c_D}{\partial M_\infty}\right|_{M=M_{DR}} = 0.1 \tag{1.6}$$

Another influential parameter is the *mass flow capture ratio* (MFCR) defined as the ratio between the cross sectional area of the streamtube entering the propulsor at upstream infinity and the highlight area:

$$MFCR = \frac{A_\infty}{A_i} \tag{1.7}$$

In general, it reaches its maximum value at take-off and climb but, during cruise phase, MFCR<1. In this case another type of drag force, named *spillage drag*, is formed. This happens when the inlet "spills" air outwards instead of directing it to the fan face. In this way the force acting in the streamtube upstream the inlet is not balanced with the forebody suction.

The study conducted by Robinson, MacManus, Sheaf [2] analysed four types of nacelle for different flight velocities, incidence angles, and exhausts.

1. Nacelle 1: axisymmetric design with cylindrical centrebody
2. Nacelle 2: design made to obtain a certain Mach number distribution on the nacelle surface
3. Nacelle 3: 3D design
4. Nacelle 4: conventional design with the adoption of UHBPR engine

For the geometries described above, the effects of the sting mount are also assessed, therefore four nacelles in three configurations are simulated using CFD analysis for a total of 14 created meshes. These three configurations concern nacelle and sting (NS), isolated nacelle (N) and nacelle with exhaust system (NE).

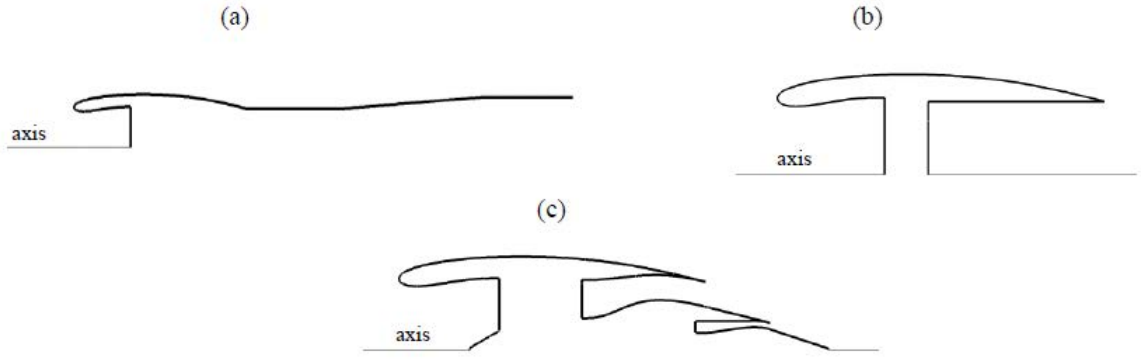

Figure 1.5: *Nacelle configurations. (a) Nacelle with sting (b) Isolated nacelle with cylindrical exhaust (c)Nacelle with exhaust system [2].*

The following table summarizes simulations cases.

	Dimension	Configuration	M_∞	MFCR	Re ($*10^6$)	AoA (°)
Nacelle 1	2D	NS	0.65-0.95	0.4-0.78	2-2.2	0
Nacelle 2	2D, 3D	NS, N	0.8-0.89	0.45-0.7	4-4.5	0-4
Nacelle 3	3D	NS, N	0.8-0.88	0.55-0.85	4.2-4.4	4-6
Nacelle 4	2D	NS, N, NE	0.7-0.9	0.55-0.75	4.5-28.9	0

Table 1.1: *Nacelles configurations analysed in [2].*

After building nacelle and domain's mesh for every configuration, drag extraction is computed. For this scope there are two methods for drag assessment in a CFD simulation: near field method and far field method. The first calculates drag in the body perspective due to pressure distribution and skin friction, while the far field method employs the flow field perspective in which drag force is due to shock waves, vortex sheet, and viscous forces. In other words, the near field method integrates pressure and viscous forces acting on the nacelle in flow direction, but it can't isolate shock waves and boundary layer displacements effects which are included in the pressure term (Equation 1.8). With the far field method one employs surface integration of a control volume which limits the component to determine drag (Equation 1.9).

$$D = \iint_S (-pn_x + \tau_{xx}n_x + \tau_{xy}n_y + \tau_{xz}n_z)dS \tag{1.8}$$

$$D = \int \dot{m}(V_\infty - V)dA \tag{1.9}$$

In 1.8, the first term represents pressure forces while the other three are viscous terms. For Equation 1.9, $\dot{m}$ is the mass flow rate, V_∞ the freestream velocity; in this case the integral has to be calculated in a region where $\dot{m}$ is known and the velocity V can be easily measured.
A more accurate method for NS configuration used in this study is based on the near field method (modified near field method) in which pressure and viscous forces on nacelle's surface and in the pre entry streamtube are integrated obtaining a modified drag and drag coefficient in which the sting's effect is taken into account too.

$$D'_{nac} = \phi_{nac} + \phi_{pre} + \phi_{sting} \tag{1.10}$$

$$c_{D'} = \frac{D'_{nac}}{\frac{1}{2}V_\infty^2 \rho_\infty A_m} \tag{1.11}$$

Where A_m is the maximum nacelle area. The last term of 1.10 is then subtracted from D'_{nac} in order to obtain the modified drag and the corrected drag coefficient c_{Dc}:

$$c_{Dc} = c_{D'} - c_{D,sting} \tag{1.12}$$

c_{Dsting} is calculated as follows:

$$c_{Dsting} = \left(\frac{A_{wc} + A_{ws}}{A_m}\right) c_{f,combined} - \left(\frac{A_{wc}}{A_m}\right) c_{f,t} \tag{1.13}$$

A_{wc} is referred to the wetted cowl, A_{ws} to the wetted sting and c_f is the skin friction coefficient of nacelle and sting combined ($c_{f,combined}$) and total skin friction coefficient ($c_{f,t}$) calculated with flat plate theory [13].

For NE and N configurations, the exit streamtube has to be considered as well, in which case, drag and drag coefficient become:

$$D_{nac} = \phi_{nac} + \phi_{pre} + \phi_{post} \tag{1.14}$$

$$c_D = \frac{D_{nac}}{\frac{1}{2}V_\infty^2 \rho_\infty A_m} \tag{1.15}$$

$$c_{D,post} = \frac{\phi_{post}}{\frac{1}{2}V_\infty^2 \rho_\infty A_m} \tag{1.16}$$

The inclusion of an exhaust system is predicted to have a significant effect on drag assessment.
Obtained results highlight the influence of both Mach number and MFCR for nacelle 1 because a lower Mach number causes a lower MFCR with the consequence of a displacement of the stagnation point towards the throat. In this way, since the stagnation point divides internal and external flow, the flux has a greater distance to travel around the lip increasing drag contribute because of the huge acceleration given by the curvature.

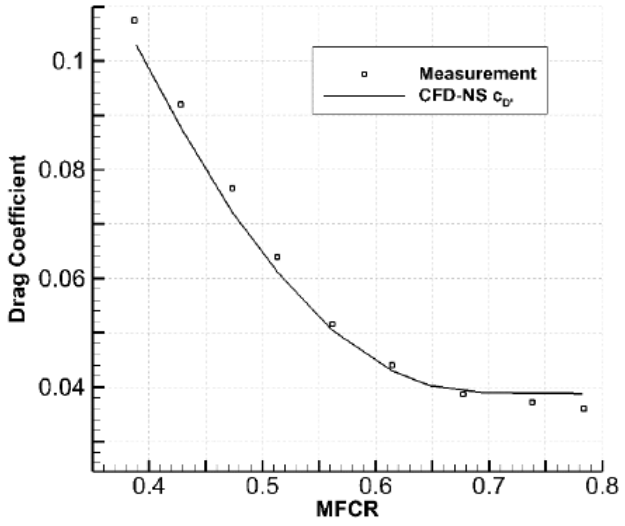

Figure 1.6: *MFCR influence on drag coefficient at* $M_\infty = 0.85$ *for nacelle 1 [2].*

Examining results related to nacelle 2 it can be seen that at a MFCR=0.7, M_{DR} is grown from a value of $M_{DR} = 0.845$ for nacelle 1 to $M_{DR} = 0.88$ for nacelle 2, this is because there is an improved control on nacelle's curvature. For the same reason at $M_\infty = 0.85$ an increase of 20% in drag occurs from MFCR=0.7 to MFCR=0.5 for nacelle 2, while the growth for nacelle 1 in the same MFCR's range and M_∞ is about 85% (Figure 1.7). For nacelle 2 and nacelle 3 also incidence angles effects are analysed. Generally, nacelle incidence leads to a displacement of stagnation point for both top and bottom surfaces, in particular the top streamline moves inside the inlet and the lower one tends to move outward. Similarly to what happens when MCFR decreases, in this situation too, the fluid has to move around the top surface cowl lip, with an increasing acceleration and consequently more drag. From drag rise Mach number perspective, as incidence angle increases, M_{DR} decreases, even though for nacelle 3 incidence effects are less pronounced.

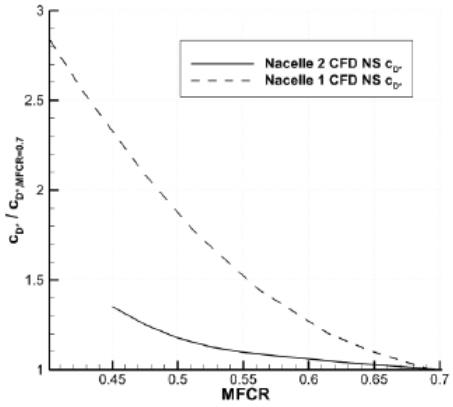

Figure 1.7: *Comparison of MFCR between nacelle 1 and nacelle 2 of normalized drag coefficient at $M_\infty = 0.85$ [2].*

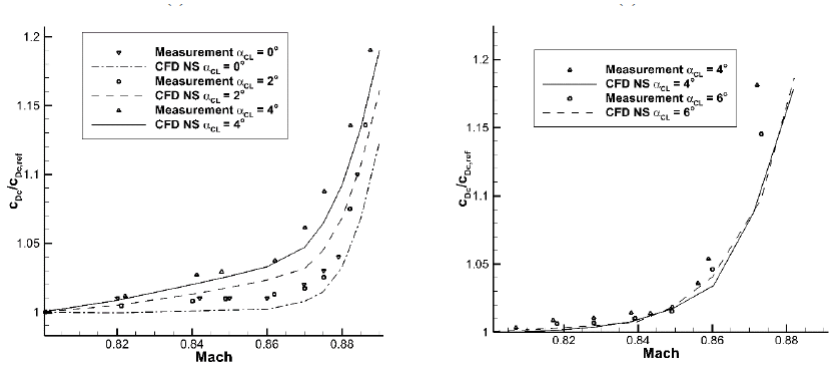

Figure 1.8: *Normalized drag coefficient for different incidence angles for nacelle 2 at MFCR=0.7 (left) and nacelle 3 at MFCR=0.75 (right) [2].*

As previously said, some configurations for exhaust systems are simulated and some differences are expected. In particular, the NS configuration has the lowest drag because the post exit term is not included, and, in fact for the NE configuration the post exit drag has a contribution of about 61% to the modified drag. Nacelle 4 also highlights a decrease in terms of drag rise Mach number for N and NE configurations with respect to NS one.

Related to the spillage drag, N and NS configurations report the highest value of spillage drag. Before considering post exit term, the NE configuration, presents the greatest modified spillage drag ($c_{D^*_{spill}}$) but including also ϕ_{post} a negative spillage drag is obtained. This occurs because a lower MFCR causes a lower nozzle pressure ratio obtaining more jet expansion, therefore the spillage can be dominated by an increased post exit force which, for a range of low MFCR, causes a lower overall drag.

1.1.2 Under-wing engines vs clean-wing aircraft

Another aspect of engine installation effects has to consider the differences between an aircraft with no engine wing and the same aircraft provided with an under-wing installed engine. In [3] installation effects are analysed in terms of comparison between clean wing and installed nacelle wing. Furthermore some axial and vertical nacelle's positions and isolated nacelle are investigated using CFD analysis.
Calculations are carried out considering the Nasa CRM at cruise phase with a Mach number of 0.82, a flight altitude of 35000 ft and AoA between 0° and 5°. Nacelle's axial and vertical positions are illustrated in Figure 1.9.

(a) *Axial analysed nacelle's positions.* **(b)** *Vertical analysed nacelle's positions.*

Figure 1.9: *Nacelle's studied positions in the presence of the wing of CRM [3].*

Investigation parameters concern drag, lift, and thrust. In particular the *Net Propulsive Force* (NPF) is calculated as the difference between the overall engine's thrust and the nacelle's drag.
As it was predictable, the installed nacelle (called through flow nacelle, TFN) increases drag coefficient, but more in general it affects lift coefficient and pressure coefficient distribution.
A simulation of a WBNP (Wing Body Nacelle Pylon) is made, where engine position is the baseline one (C3). Clearly, installation effects are evident. Referring to c_p distribution over the wing, in Figure 1.10, the displacement of the shock wave from x/c=0.45 for the clean wing to x/c=0.35 for the wing with installed nacelle is visible.

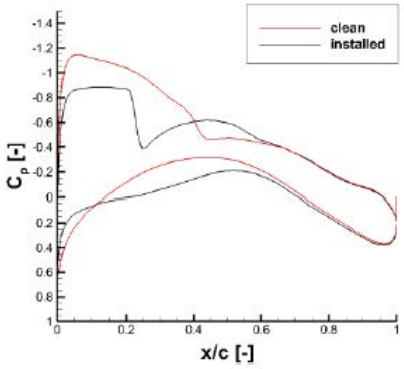

Figure 1.10: c_p *distribution for WB (clean wing) and WBNP at* $M_\infty = 0.83$ *[3].*

In this study also, incidence angle effects are analysed because installation effects depends also to AoA which range is from AoA=0° to AoA=5°. If also lift coefficient as a function of drag coefficient is considered, the great interaction between wing and nacelle is notable (Figure 1.11).

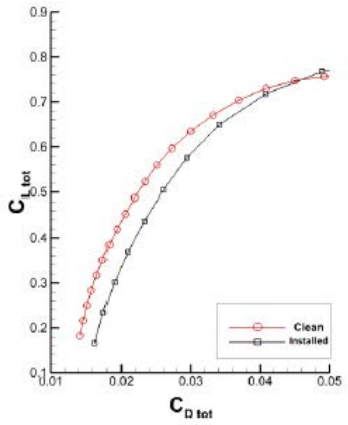

Figure 1.11: *c_L behaviour as a function of c_D with the baseline engine position C3 at $M_\infty = 0.82$ [3].*

To better quantify overall effects, thrust is considered in terms of GPF_ξ that is the gross propulsive force directed to the engine axis and the comparison is made between an installed nacelle and an isolated nacelle. As a result, since the GPF is a function of incidence angle, for a $\text{AoA}_{A/C}$ of 2.5°, GPF is reduced of about 0.1% and with $\text{AoA}_{A/C}$ of 4° the reduction of GPF increases until 0.25% if compared to the isolated nacelle. This discrepancy could be linked to the presence of the wing which exerts a pressure field on exhaust's external surfaces.

Engine axial position can lead to several changes with regards to the clean wing. As it is shown in Figure 1.12, at a typical cruise condition of $c_L = 0.5$, installation effects are not negligible. Thus, to better appreciate the influence of the three axial positions the so called installation drag is computed:

$$\Delta c_{D,inst|CL} = [c_{D,installed} - c_{D,clean}]_{c_L=const} \tag{1.17}$$

Installation drag represents the difference in drag coefficient among installed nacelle and clean wing at a constant lift coefficient. This value is 43 dc,43 dc and 38 dc for A1,B1,C1 respectively at $c_L = 0.5$. Despite at high lift coefficient values, c_D behaviour is quite the same, there are instead significant differences at $c_L = 0.2$ where, for C1 position, more interaction between wing and nacelle is visible. This influence is clearer focusing on Mach contours in which clean wing, isolated nacelle, and wing+nacelle configurations are compared.
For future engine technologies and designs, it is useful to consider nacelle's vertical position too. Referring to Figure 1.9 (b), CFD simulation results highlight an increasing installation drag (Equation 1.17) from C1 to C3 at $c_L = 0.2$ of about 20 dc but considering the typical cruise phase in which $c_L = 0.5$, installation drag reaches 38 dc for C1 and 34 dc for C3.

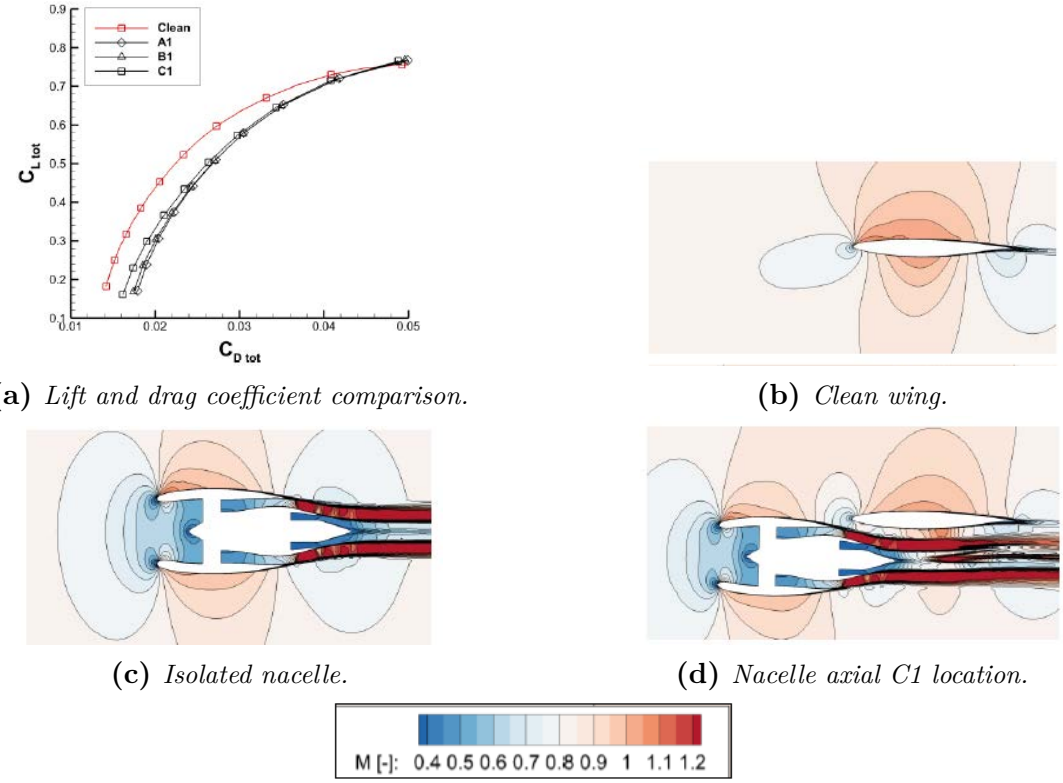

(a) *Lift and drag coefficient comparison.*

(b) *Clean wing.*

(c) *Isolated nacelle.*

(d) *Nacelle axial C1 location.*

Figure 1.12: *Lift and drag coefficient behaviours for all axial locations and Mach contours for (b) clean wing (c) isolated nacelle and (d) installed C1 nacelle and wing [3].*

Even though total drag doesn't exhibit huge differences amongst vertical nacelle's locations, the best choice in total drag terms is C3. Focusing instead on GPF_{ξ}, all positions illustrate a decreasing trend if compared with the isolated nacelle at $\mathrm{AoA}_{A/C} = 2.5°$ because of the pressure field exerted by the wing.

Concluding, the addition of the installed nacelle leads unavoidably to an increased drag, the magnitude of which depends on flight condition, incidence angle, and nacelle's position. Even though drag assessment, as estabilished, is of fundamental importance, the installation design also has another important element to consider: thrust in terms of gross propulsive force. This because of the interaction between wing pressure field and exhaust system, which makes GPF vary due to nacelle's and wings' relative positions.

1.2 Ultra Short Nacelles

As referred to earlier, future civil aircraft engine designs are concerned with higher bypass ratio and lower total pressure ratio fans in order to reduce emissions and noise, as well as improving propulsive efficiency. Since bypass ratio is defined as the ratio between the mass flow rate of the bypass stream (cold airflow) and the mass flow rate that passes through the core engine (hot airflow), increasing its value means augmenting cold airflow with respect to the hot airflow which will be then processed by the core engine.
Future engines will employ BPR above 15 [14] while currently values of bypass ratio are about 10/11. Higher values of B imply larger engine diameters, which lead to an increase in drag and weight. The compromise between these various aspects is the adoption of *Ultra Short Nacelles*, characterized by a shorter inlet to minimize the impact of large diameter fans on nacelle's weight and drag. A critical aspect of shorter inlets is a minor internal diffusion capability, they could worsen inlet distortion decreasing fan performances [4].
However, the analysis conducted in [4] shows how to improve overall drag by shortening nacelle inlet from the traditional value of L/D=0.5 to lower values. On the other hand,

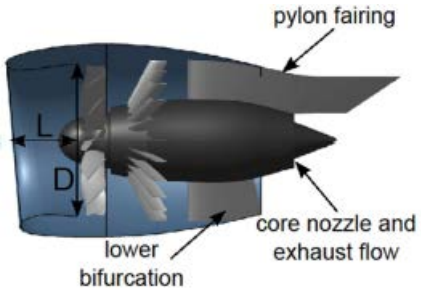

Figure 1.13: *Baseline propulsor configuration [4].*

shortening too much the nacelle length is not the best choice because, for L/D<0.25, the benefits achieved in terms of drag reduction are offset by an efficiency penalty. Therefore the suggested range is between L/D=0.25 and L/D=0.4.
The most critical challenge in short nacelle design is to find a compromise in terms of L/D values. The aim is to obtain high fan rotor adiabatic efficiency while also reducing nacelle drag because, when the inlet is shorter, fan efficiency starts decreasing due to inlet distortion mechanisms. At the same time though, this leads to lower drag and higher pressure recovery, two aspects that make propulsive efficiency increase.

1.2.1 Design aspects

When designing nacelles, there are some flight conditions to consider and the main target is to achieve a trade-off design which evaluates both cruise and off-design performances. Especially, those considered in [4] are:

- Cruise aerodynamic design point (ADP): in this condition there is an angle of attack (AoA) of 5° because of the wing upwash that leads to an inclination of nacelle

highlight area to flow direction.

- Wing C_{Lmax}: in this case the AoA is 29°, even if this situation is not normally encountered during flight.
- Cross wind: inlet flow separations and high inlet distortions are the most problematic aspects.
- Take-off rotation, in which inlet non-uniformities penalize fan efficiency.
- Take-off level: the situation just before take-off rotation.

Nacelle design has to consider both wave drag due to maximum external Mach number at cruise condition [13] and flow separations coupled with inlet distortions at off-design conditions.
Airflow around nacelle top and bottom sections behaves in different ways for each flight condition, therefore their geometric shapes have to be separately designed.

For the top section the design philosophy is based on *Supercritical Airfoils* [15], which allow a wave drag reduction because of less flow acceleration in cruise condition: this is obtained by aligning external nacelle surface with the streamtube that divides internal and external flow (Figure 1.14). As it can be seen, at cruise the mass flow capture ratio (MFCR), is lower than unity and the stagnation point shifts towards the internal part of the inlet lip.

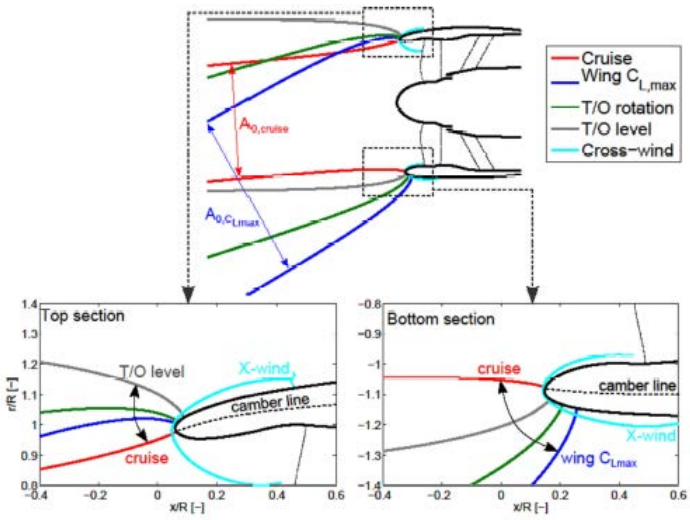

Figure 1.14: *Example of streamtubes at each flight condition for short-inlet design of L/D=0.19 [4].*

In terms of lip thickness, this must be thin enough to avoid high wave drag but thick enough to prevent flow inlet separation. The most critical situation occurs at T/O Level, in which the stagnation point moves outward on the nacelle external surface, so lowest lip thickness value at the top nacelle surface is the one which guarantees separation-free inlet flow at T/O Level.
Considering the bottom section, the design strategy carried out in [4] consists in an inlet bottom elliptical shape with a thicker lip in order to avoid flow separation, consequently

high distortion at low speed, especially at C_{Lmax} condition, where there is the maximum shift of the stagnation point (visible in Figure 1.14).

Mach number considerations

An important difference between long and short inlets consists in flow area evolution through the inlet.
For compressible fluids, section area is directly linked to Mach number by *Rankine-Hugoniot* equation:

$$\frac{dA}{A} = \frac{dc}{c}(M^2 - 1) \tag{1.18}$$

From Equation 1.18 some aspects can be deduced [16]:

1. For subsonic speed (M<1):
   - dA>0 ⇒ dc<0
   - dA<0 ⇒ dc>0
2. For supersonic speed (M>1):
   - dA>0 ⇒ dc>0
   - dA<0 ⇒ dc<0

In long-inlet baseline configurations, the section area decreases until its minimum value at throat, then it increases until spinner LE and it decreases until the fan face. Since Mach number is lower than one, according to Equation 1.18, airflow reaches its maximum acceleration near the throat, far upstream from fan face. While maximum averaged Mach number is reached at fan face, long inlet configuration permits flow straightening from distorted condition due to inlet flow AoA which leads to reducing rotor losses.
In short inlets, spinner LE is located near the highlight section, so flow area monotonically decreases; consequently the maximum flow acceleration location is near the fan face leading to an enhancement of distortion and increased rotor penalties.

1.2.2 Final nacelle design

As previously said, top and bottom nacelle sections have to achieve different targets, therefore it is obvious that their geometric shapes have to be different. In this regard, the inlet nacelle part is not axisymmetric. Starting from this point, several geometries have been simulated using the body force approach. From analysis conducted in [4], only one nacelle geometry has been chosen because it achieved the following targets:

- $M_{max} \simeq M_{max,baseline}$ at cruise condition
- Separation-free at low speed
- Limited distortion at off-design conditions

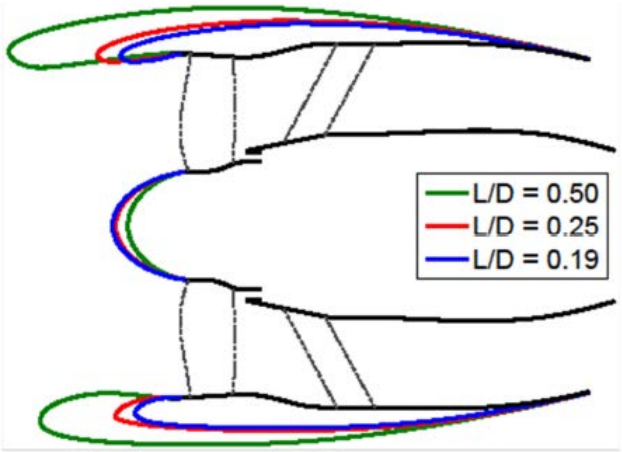

Figure 1.15: *Nacelle tested designs [4].*

Chosen design concerns L/D=0.25. This configuration leads to a reduced drag of 16%, while propulsive efficiency has almost been unchanged with respect to the baseline configuration of L/D=0.5 (the reduction is only of 0.01%). However fan efficiency decreased of 0.96%.
In Figure 1.15 also the L/D=0.19 inlet design is depicted: with this configuration higher drag reduction (17.8%) is obtained but this benefit is offset by flow separation at $C_{L,max}$ condition and by severe fan efficiency losses (-1.63%) because of incidence distortion.

1.3 Turbomachinery

Turbomachinery plays an important role in engineering. Turbomachines are machines which impart or extract energy from a continuously moving stream of fluid.
These devices can be classified on the basis of energy conversion:

- Produce power by expanding fluid to a lower pressure.
- Absorb power in order to increase fluid's pressure.

On the basis of the fluid's path:

- Axial flow turbomachines: fluid path is mainly parallel to the rotation axis.
- Radial flow turbomachines: fluid path is mainly in radial direction. They are also divided into two types: centrifugal and centripetal.
- Mixed flow turbomachines: both axial and radial flows are present.

Lastly, on the basis of the nature of the processed fluid:

- Compressible
- Incompressible

1.3.1 Axial Compressors

In an axial compressor, the working fluid flows parallel to the rotation axis. The fluid passes through rotating blades (rotors), which convert mechanical energy in terms of static temperature increase, absolute velocity therefore total temperature, and stationary blades (stators). With a decrease in relative velocity, there is an increase in static pressure. In stator blades total pressure decreases because of friction losses like absolute velocity, so static pressure increases [1].
However, is it also possible to have other stator blades upstream the first rotor blade row: this configuration is called Inlet Guide Vanes (IGV) and is used to deflect velocity by reducing the relative speed component. In addition, a stator blades row can be added downstream the compressor (OGV, Outlet Guide Vanes) for structural reasons and to reduce fluid's swirl [1].

The compressor's purpose is to increase fluid pressure to ensure right value enters in the combustion chamber. To do that, this turbomachine has to absorb the lowest mechanical power, so isentropic efficiency has to be the highest possible.
Isentropic efficiency is defined as:

$$\eta_{is} = \frac{L_{is}}{L} = \frac{T^0_{2is} - T^0_1}{T^0_2 - T^0_1} \tag{1.19}$$

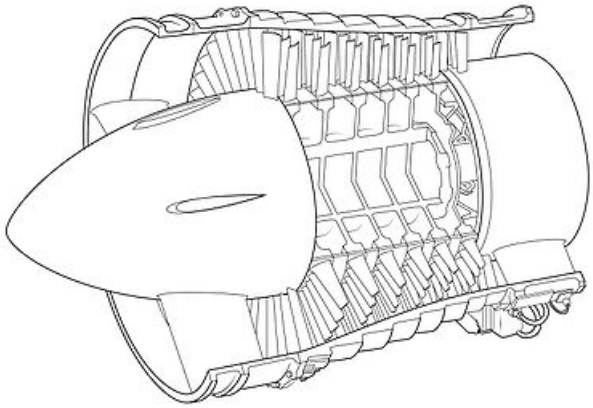

Figure 1.16: *An example of an axial compressor [17].*

In particular this one is called total-to-total efficiency because total quantities are utilized. T_1^0 is the total temperature upstream the compressor, T_2^0 the total temperature downstream the compressor and T_{2is}^0 the total temperature reachable in the hypothesis of isentropic process. It must be specified that, in general, $L = \Delta h^0 = c_p \Delta T^0$.
This parameter can be written also in terms of total pressure ratio π_c:

$$\eta_{is} = \frac{\pi_c^{\frac{k-1}{k}} - 1}{T_2^0/T_1^0 - 1} \tag{1.20}$$

π_c is the ratio between total pressure downstream and upstream the compressor.

$$\pi_c = \frac{p_2^0}{p_1^0} \tag{1.21}$$

Another way to establish machine efficiency is by introducing polytropic efficiency. This parameter does not depend to the pressure ratio so it better describes the real performances of the machine. Referring to Figure 1.17 it can be noticed that if the exit temperature (enthalpy) augments, the value of L increases as a consequence. In this way it seems that isentropic efficiency value reduces because of the link between pressure ratio and work.
Polytropic efficiency does not depend on total pressure ratio and it is the best way to judge machine efficiency level.

$$\eta_{pol,c} = \frac{\frac{k-1}{k}\log(\pi_c)}{\log\left(\frac{T_2^0}{T_1^0}\right)} \tag{1.22}$$

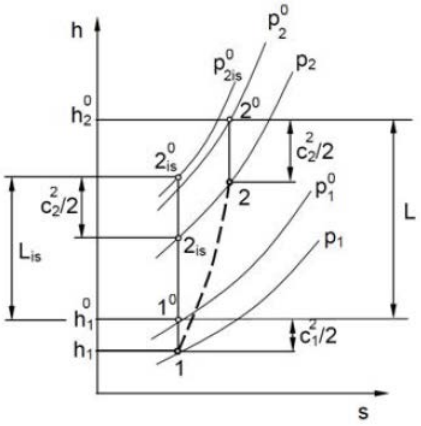

Figure 1.17: *Thermodynamics of compression process [5].*

In order to better understand next chapters, characteristic maps are introduced. They are curves which describe machine performances; these maps are obtained experimentally and show total pressure ratio and isentropic (adiabatic) efficiency varying mass flow rate and rotational speed. In Figure 1.18 an example is illustrated.

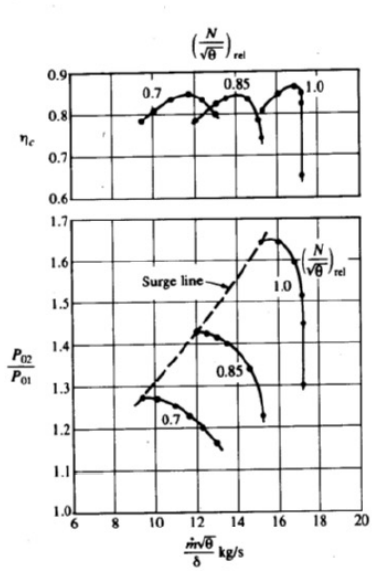

Figure 1.18: *Characteristic compressor maps [5].*

Referring to dimensional analysis, mass flow rate and rotational speed can be expressed in terms of corrected mass flow rate ($\dot{m}_c$) and corrected speed (N_c) respectively.

$$\dot{m}_c = \frac{\dot{m} \cdot \sqrt{\theta}}{\delta} \tag{1.23}$$

$$N_c = \frac{N}{\sqrt{\theta}} \tag{1.24}$$

Where $\theta = T_1^0/T_{1,ref}^0$ and $\delta = p_1^0/p_{1,ref}^0$. In particular $T_{1,ref}^0 = 288.15$ K, $p_{1,ref}^0 = 101325$ Pa. We can notice that each speed line presents two limits: on the left there is the *surge*

(or stall) line and on the right there is the *choke line*; these two lines represent limits in terms of mass flow rate. Indeed, the first corresponds the minimum mass flow rate to avoid instabilities and stall, the latter represents the maximum mass flow rate: the speed line close up rapidly and beyond the choke any further increase in speed generates no further increase in mass flow rate.

- II -

Validation and Model Setup

As described in the previous chapter, the first step of this thesis is to validate a CFD model of NASA Rotor 67 geometry using TurboGrid and CFX; obtained CFD results are compared with experimental data available in the NASA report [6]. The present chapter continues with the entire model description (nacelle+spinner+blade) and case setup.
Before facing this topic, a brief description of transonic blades is introduced.

2.1 Transonic Compressor Rotors

In aeronautics, the most important targets to achieve is weight and fuel burn reduction. According to this, instead of classical subsonic stages, transonic axial compressors and fans are now widely used because of their compactness and reduced costs.
In a transonic stage, the lower part of the blade is characterized by a subsonic airflow, while the upper part faces a relative supersonic flow field. If well designed, these kind of stages could guarantee a higher total pressure ratio than that reached by subsonic ones; consequently if a certain value of pressure ratio has to be reached, employing a transonic compressor means less number of necessary stages, therefore this leads to less total weight. Despite subsonic stages have higher values of efficiency, transonic ones reach high efficiency levels too (about 90%), which means fuel reduction.
A single-stage transonic fan has become a basic element for high bypass ratio civil engines because it is able to produce the majority of the total thrust as well as it can largely influence fuel burn and noise [18].

2.1.1 Nasa Rotor 67

NASA rotor 67 is a high-speed axial flow compressor rotor originally tested at the NASA Glenn Center [6].
It is the first stage rotor of a two stage transonic fan with 22 blades and aspect ratio of 1.56 based on average span/root axial chord.
R67 rotational design speed is 16043 RPM, with tip leading edge speed of 429 m/s and a tip relative Mach number of 1.38. Other features of NASA Rotor 67 are summarized in Table 2.1.

Experimental data are available near peak efficiency and near stall points. A laser anemometer technique was used to measure tangential and axial velocities with 50 points

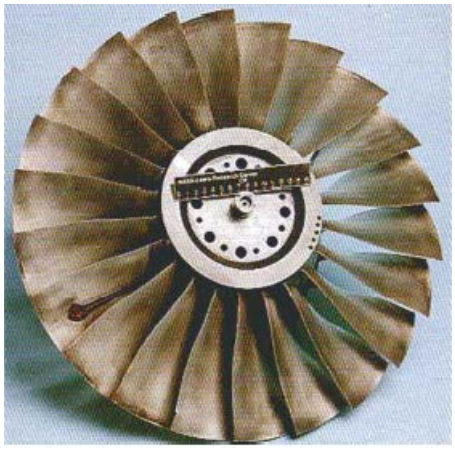

Figure 2.1: *NASA Rotor 67 configuration.*

Number of blades	22
Design rotational speed [RPM]	16043
Tip speed [m/s]	429
Inlet tip relative Mach number	1.38
Design mass flow rate [kg/s]	33.25
Mass flow rate at choke [kg/s]	34.96
Design pressure ratio	1.63
Tip clearance [mm]	1.016
Average aspect ratio	1.56
Tip solidity	1.29
Hub solidity	3.11
Tip radius at LE [cm]	25.7
Tip radius at TE [cm]	24.25
Inlet hub to tip radius ratio	0.375
Outlet hub to tip radius ratio	0.478

Table 2.1: *NASA Rotor 67 specifications.*

in θ direction (blade-to-blade direction), while radial and axial positions were fixed.
The obtained data are available in two kinds of plots: streamwise plots with fixed pitch and blade-to-blade plots at a fixed chord. Relative Mach number and relative flow angle are measured. Other data consist in contour plots of relative Mach number at 10%, 30% and 70% span from shroud. In addition, data about total and static pressure, total temperature and flow angle upstream and downstream the rotor were collected.
Further details can be found in [6].

2.2 Validation

The geometry comprises 14 spanwise blade sections which will be read by the mesher in order to create blade geometry.

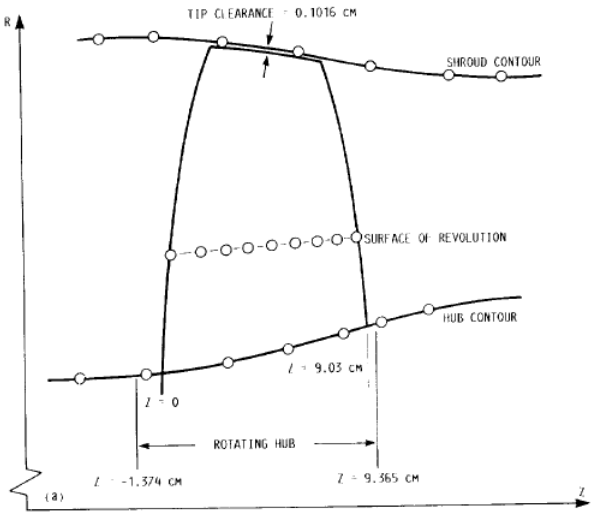

Figure 2.2: *Meridional representation of NASA Rotor 67 [6].*

2.2.1 Grid

As previously said, the mesher code used is ANSYS Turbogrid and to create the geometry it needs three file .curve (hub.curve, shroud.curve and blade.curve). The main parameters used to create the mesh have been deducted from other validation cases of NASA Rotor 67 ([19], [7], [20]).
Inlet, passage and outlet have to be meshed. The most critical block is the passage because of the blade presence.
The topology set is made with the Automatic Topology and Meshing (ATM Optimized), which guarantee an high quality mesh and generates a structured mesh. In order to reduce mesh distortions along the spanwise direction of the blade, 10 layers are created (Figure 2.4).
Figure 2.5 shows layers of hub and tip sections.

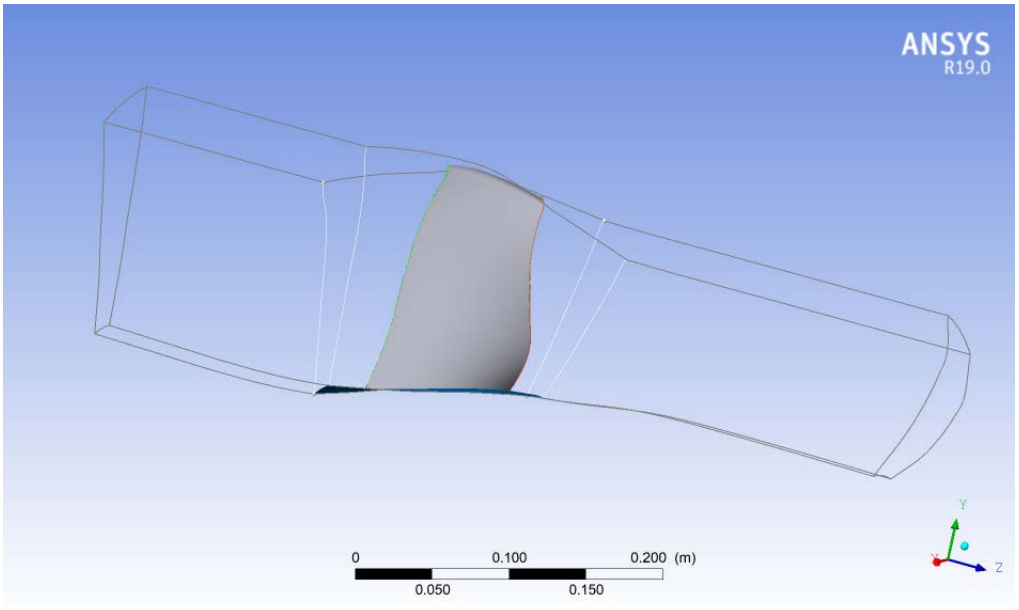

Figure 2.3: *Inlet, Outlet and Passage blocks.*

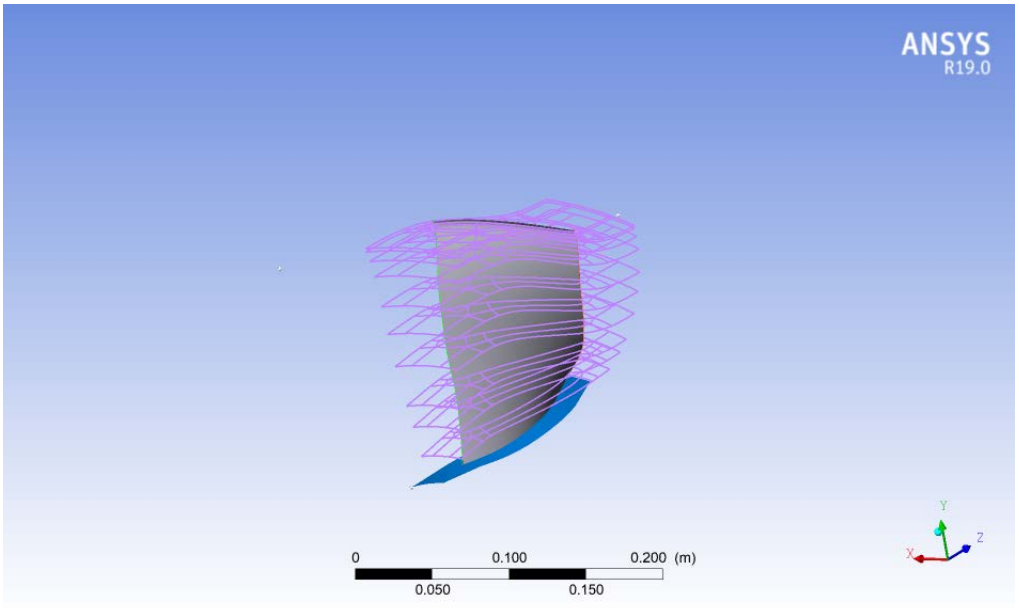

Figure 2.4: *Layers along the span.*

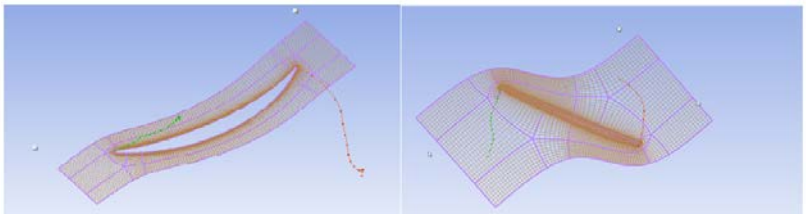

Figure 2.5: *Hub (left) and tip (right) sections.*

To build the mesh, target passage mesh size method with 1.7M specified value is adopted, with this method a target number of nodes in the mesh passage can be chosen, so if spanwise mesh size or boundary layer refinement are changed, TurboGrid adjusts the mesh in order to achieve the target specified number of nodes. For boundary layer refinement control, the chosen method is first element offset that allows a direct control of the first row of elements near the blade, offset Y+ imposed was 1, target maximum expansion rate was 1.3 and the near wall element size specification utilized method was y+. This option permits the control of the near-wall node spacing (distance between a node and the first layer of nodes from the wall). The imposed reference Reynolds number was 2.5e+06.
For the passage block in the spanwise direction a number of 110 elements is imposed. Across the tip gap 42 elements were specified using *uniform* method, which creates same size elements.
Inlet and outlet blocks are characterized by H-grid topology and they have respectively 28 and 34 streamwise elements. In this way there's no need to control target expansion rate because it is determined by the number of elements.
The resulting mesh is about 2.1M elements.

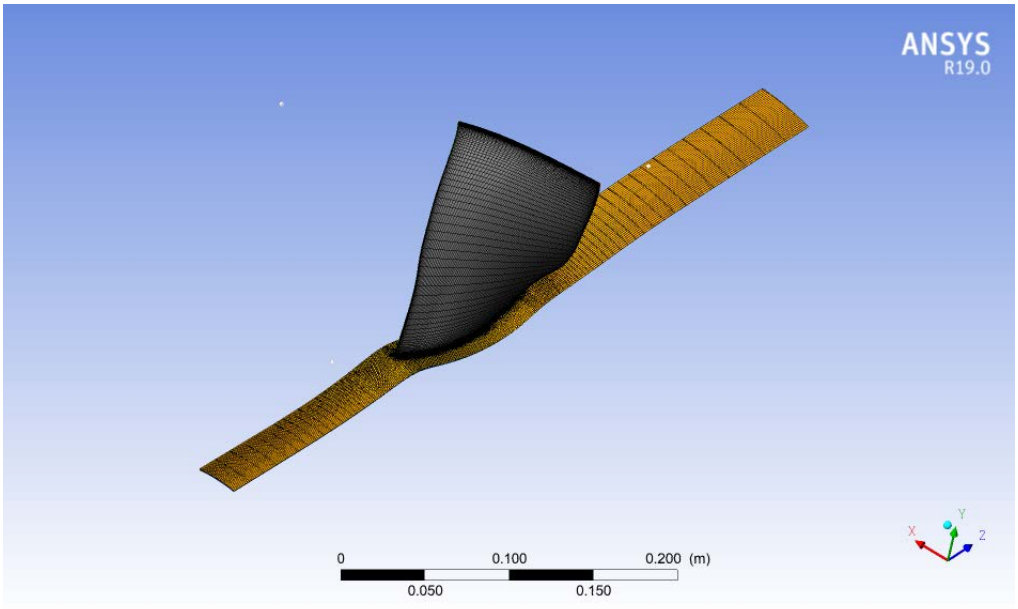

Figure 2.6: *Final mesh.*

2.2.2 CFX-Pre

The mesh created in TurboGrid has then been imported into CFX-Pre (the pre-processor of ANSYS CFX). Concerning with turbulence phenomenon, three different approaches could be adopted:

1. RANS-Reynolds Averaged Navier-Stokes Simulation: it solves RANS equations by using different types of closure models. Computational costs are reasonable.
2. DNS-Direct Numerical Simulation: this method solves Navier-Stokes equations in a direct way, therefore computational costs are really unaffordable.
3. LES-Large Eddy Simulation: a compromise between RANS and DNS, however computational costs are too time-expensive.

In CFX, RANS equations are solved. Since the flow presents turbulence phenomena, the best choice for RANS closure model was $k-\omega-SST$, which is a combination of $k-\varepsilon$ and $k-\omega$ models. The first works best in the farfield, while the other near the blade. This closure model requires a y+ value lower than unity. y+ is defined as:

$$y+ = \frac{u^* \Delta s}{\nu} \tag{2.1}$$

It is the dimensionless wall distance. In particular ν is the kinematic viscosity, Δs the wall spacing and u^* is the friction velocity.
Only one blade passage is analysed for the validation.
CFX-Pre settings which have been used are:

- Basic Settings:
  - Machine Type: Axial Compressor
  - Rotation Axis: z
- Component Tipe: R1
  - Type: Rotating
  - Value: -16043 [RPM]
  - Tip clearance at shroud: yes
- Phisics Definition:
  - Fluid: Air Ideal Gas
  - Analysis Type: Steady State
  - Reference Pressure: 0 [Pa]
  - Heat Transfer: Total Energy
  - Wall Function: Automatic, High Speed (Compressible) Wall Heat, Transfer Model

- Turbulence: Shear Stress Transport
- Inflow Boundary Template:
  - P-Total: 101325 [Pa]
  - T-Total: 288.2 [K]
  - Flow Direction: Normal to Boundary
- Outflow Boundary Template:
  - P-Static: 114500 [Pa]
- Solver Parameters:
  - Advection Scheme: High Resolution
  - Convergence Control: Auto Timescale
  - Time Scale Option: Conservative
- Solver Control:
  - Advection Scheme: High Resolution
  - Turbulence Numerics: High Resolution
  - Convergence Control: Maximum Iterations 750
  - Fluid Timescale Control: Maximum Timescale 1e-07
  - Convergence Criteria:
    - Residual Type: RMS
    - Residual Target: 1e-05

CFX-Pre is provided with Turbo Mode in order to facilitate turbomachinery simulations. In this case, convergence was not so easy to reach, indeed during the calculation the maximum timescale has to be changed. In particular, since first iterations are the most unstable, an initial maximum timescale of 1e-07 with 750 iterations has been imposed, then maximum timescale has been increased to 1e-06 and finally it reaches the value of 1e-05.
When the simulation begins, some plot monitors are visible: these plots describe RMS trend. However, other plot monitors are created:

1. **Total Pressure Ratio** defined with the expression: **massFlowAve**(Total Pressure in Stn Frame)@R1 Outlet/**massFlowAve**(Total Pressure in Stn Frame)@R1 Inlet
2. **Inlet Mass Flow**: **massFlow**()@R1 Inlet
3. **Outlet Mass Flow**: **massFlow**()@R1 Outlet

Other two important default plot monitors are present: they are isentropic efficiency trend and polytropic efficiency trend (Equation 1.19 and Equation 1.22 respectively).

2.3 Validation Results

The post-processing is made by using ANSYS CFD-post.
For the purpose of reproducing the 100% rotational velocity speed line, various simulations with different values of outlet static pressure are carried out; in particular the maximum imposed value is 122000 Pa (near stall condition) and the minimum 100000 Pa (choking condition).
The following figure depicts NASA R67 obtained speed line at 100% design rotational speed of 16043 RPM.

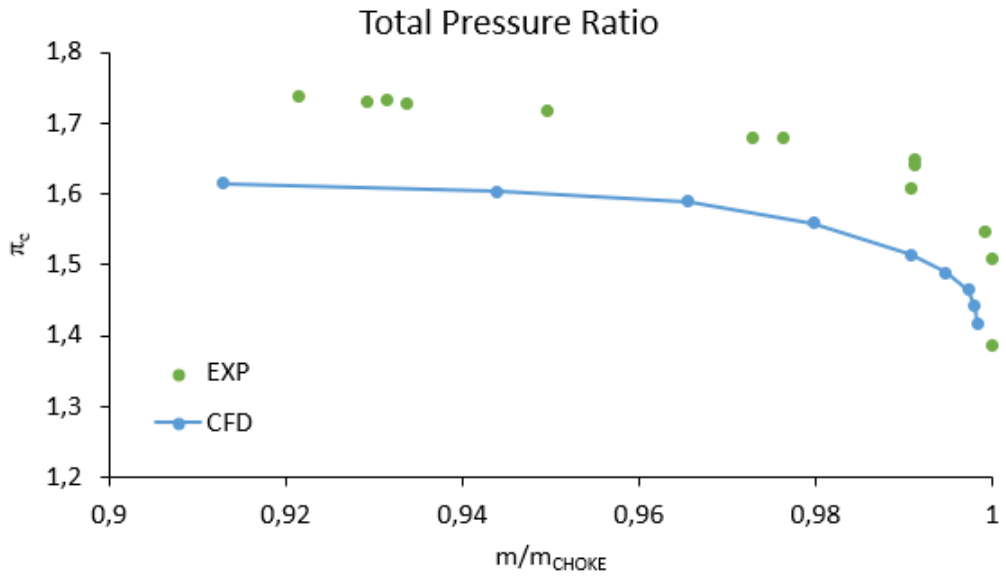

Figure 2.7: *NASA Rotor 67 speed line at 100% design speed.*

X-axis presents the normalized mass flow rate ($\dot{m}/\dot{m}_{CHOKE}$), y-axis the total pressure ratio computed as described in Equation 1.21.
Figure 2.8 illustrates obtained CFD simulation results for isentropic efficiency behaviour against normalized mass flow rate.
Despite the deviation between experimental data and CFD data, both plots present similar trends compared with experimental results. In order to better appreciate CFD simulation results, the calculation of relative errors is useful:

	CFD	EXP	Relative Error
$\dot{m}_{DESIGN}$ [kg/s]	34.10	33.25	2.5%
$\dot{m}_{CHOKE}$ [kg/s]	34.90	34.96	0.6%
$\pi_{C,DESIGN}$	1.56	1.63	4%

Table 2.2: *Comparison between CFD results and experimental data.*

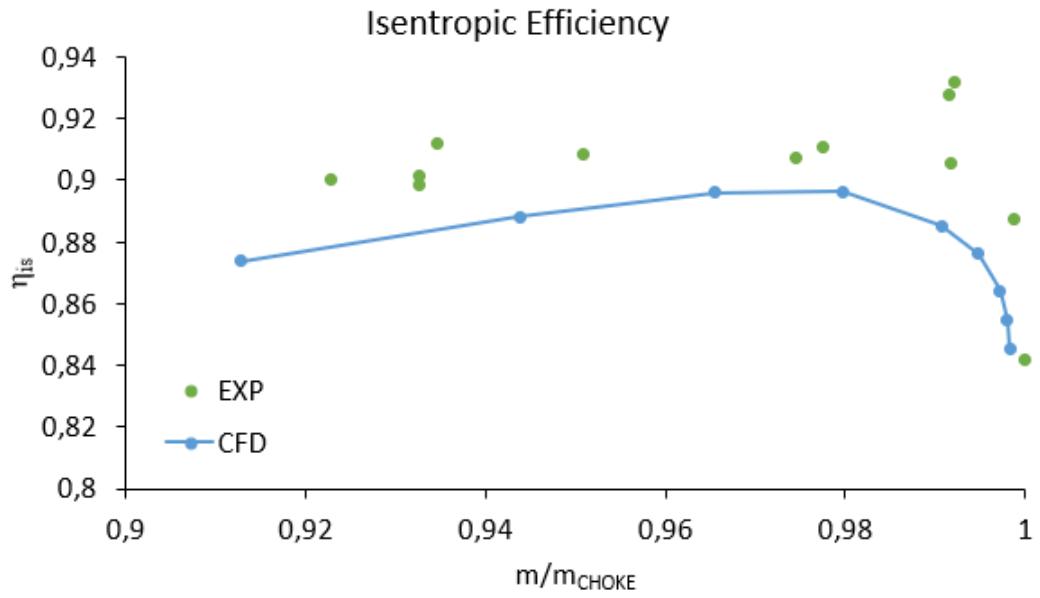

Figure 2.8: *R67 isentropic efficiency at 100% design rotational speed.*

As previously said, available data concerns near stall and near peak efficiency points. However, some results for choking condition are illustrated too.
The following figures show comparisons between Mach contours near peak efficiency point for three different span values:

1. 30% span
2. 70% span
3. 90% span

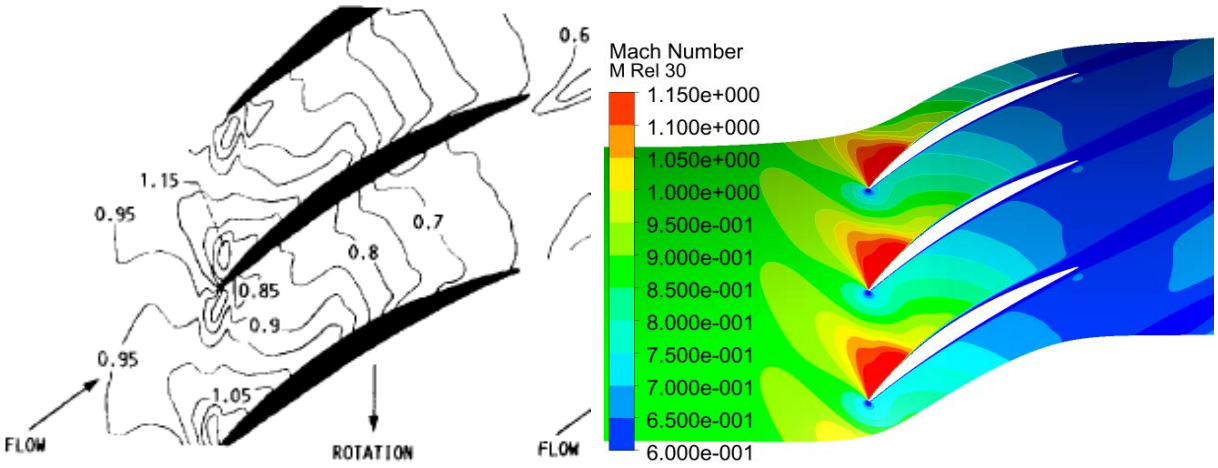

(a) *Exp Mach contours near peak efficiency.* **(b)** *CFD Mach contours near peak efficiency.*

Figure 2.9: *Mach contours comparison between CFD results and experimental data at 30% span.*

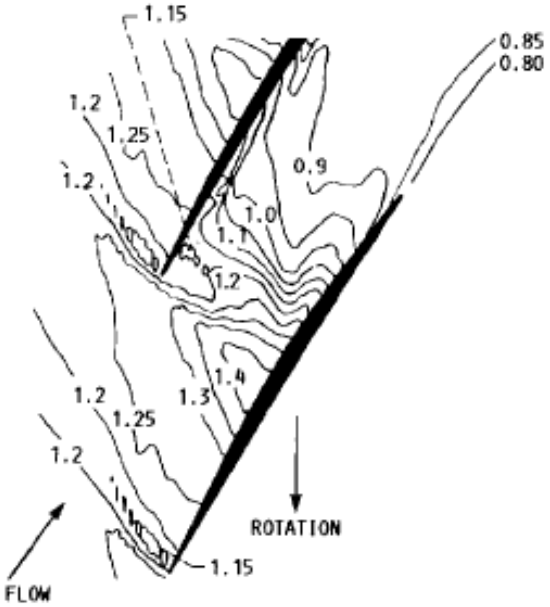

(a) *Exp Mach contours near peak efficiency.*

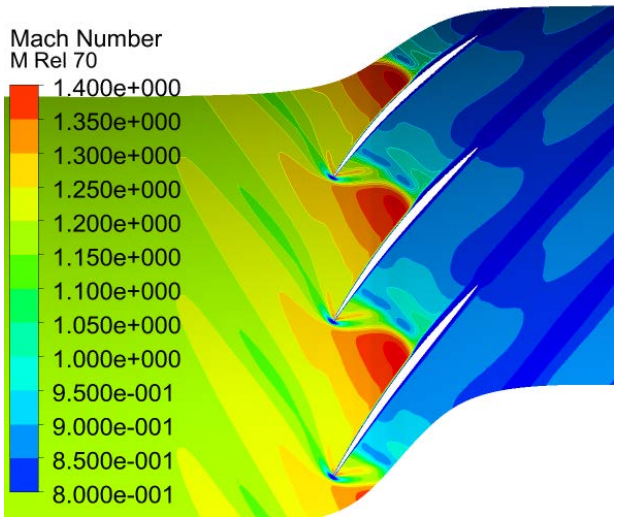

(b) *CFD Mach contours near peak efficiency.*

Figure 2.10: *Mach contours comparison between CFD results and experimental data at 70% span.*

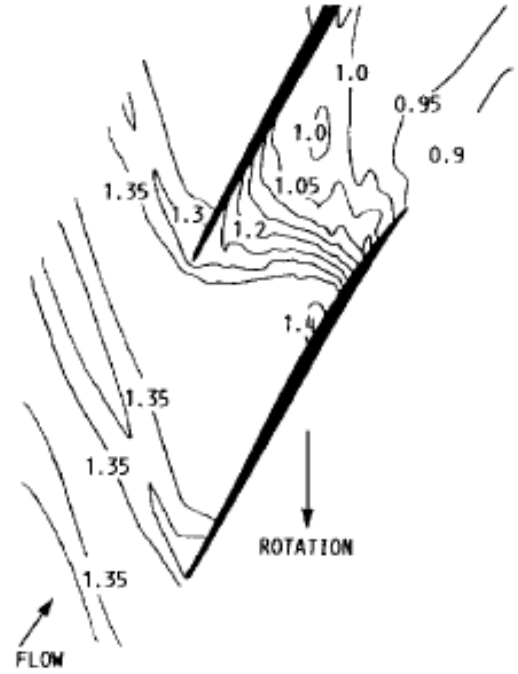

(a) *Exp Mach contours near peak efficiency.*

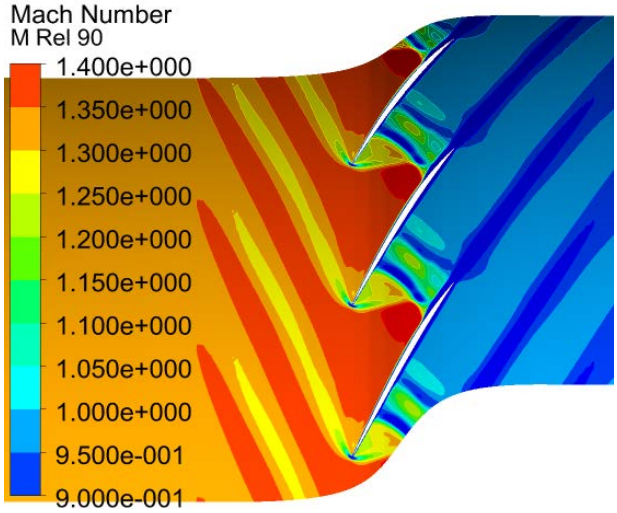

(b) *CFD Mach contours near peak efficiency.*

Figure 2.11: *Mach contours comparison between CFD results and experimental data at 90% span.*

As it can be seen, shock waves occur at the leading edge of the blade. Downstream the shock wave, Mach number is lower than unity and no other shock occurs in the channel between the blades (clearly visible especially at 90% span).
Near stall Mach number contours are shown below:

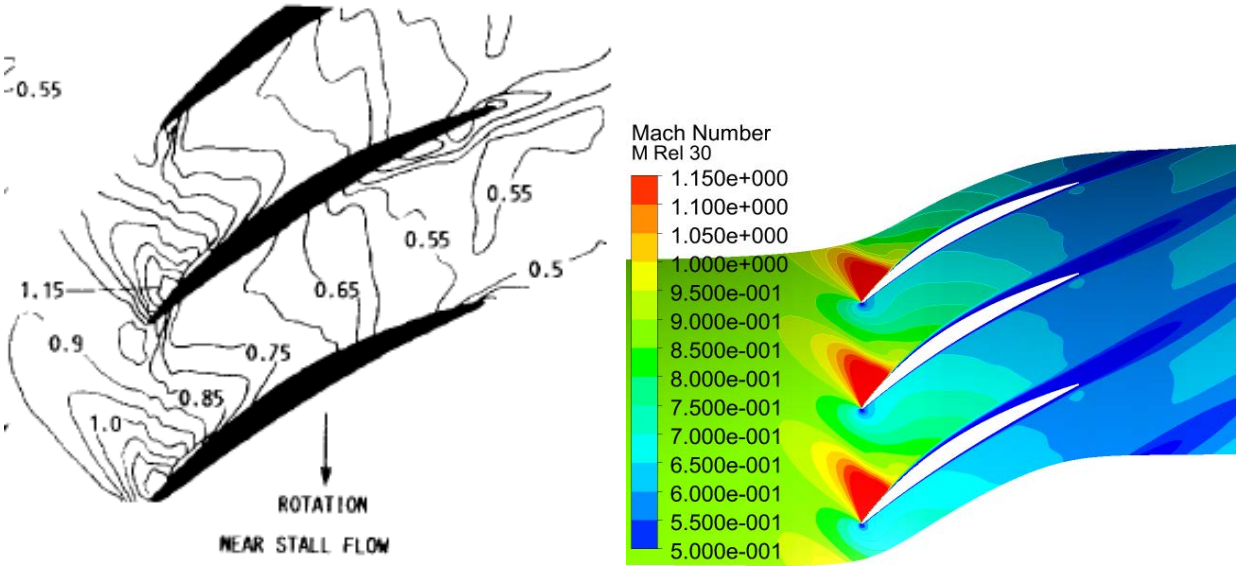

(a) *Exp Mach contours near stall.* **(b)** *CFD Mach contours near stall.*

Figure 2.12: *Mach contours comparison between CFD results and experimental data at 30% span.*

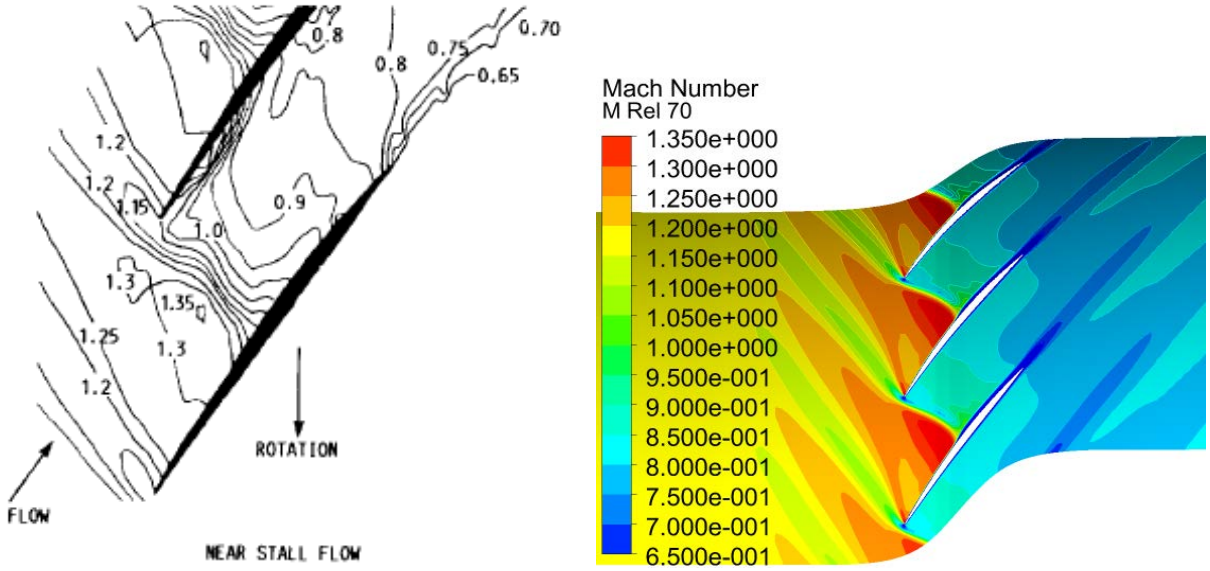

(a) *Exp Mach contours near stall.* **(b)** *CFD Mach contours near stall.*

Figure 2.13: *Mach contours comparison between CFD results and experimental data at 70% span.*

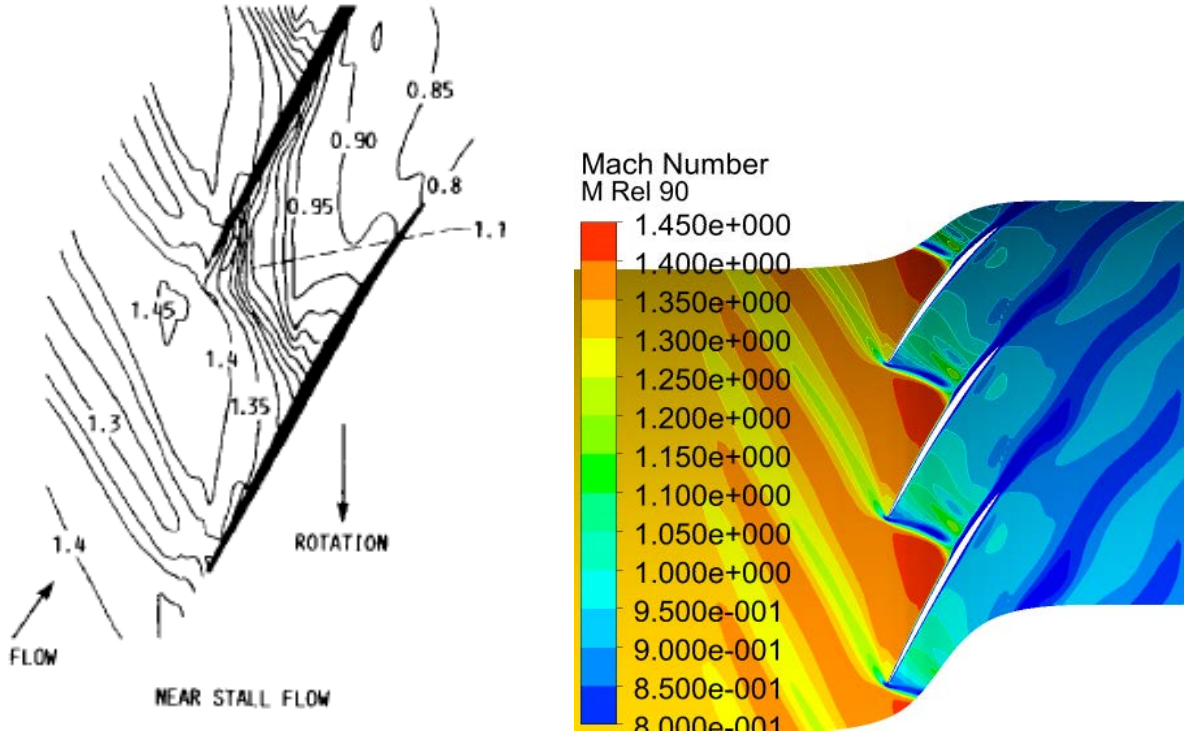

(a) *Exp Mach contours near stall.* **(b)** *CFD Mach contours near stall.*

Figure 2.14: *Mach contours comparison between CFD results and experimental data at 90% span.*

Also total temperature ratio is reported, in particular this parameter is the ratio between total temperature at station 2 and total temperature at station 1 (Figure 2.15).

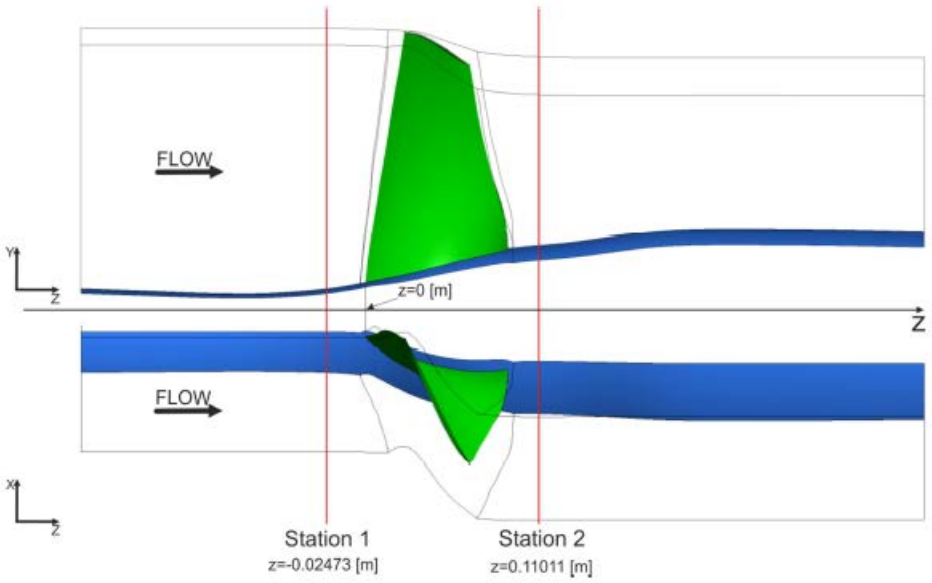

Figure 2.15: *Stations for parameters computing [7].*

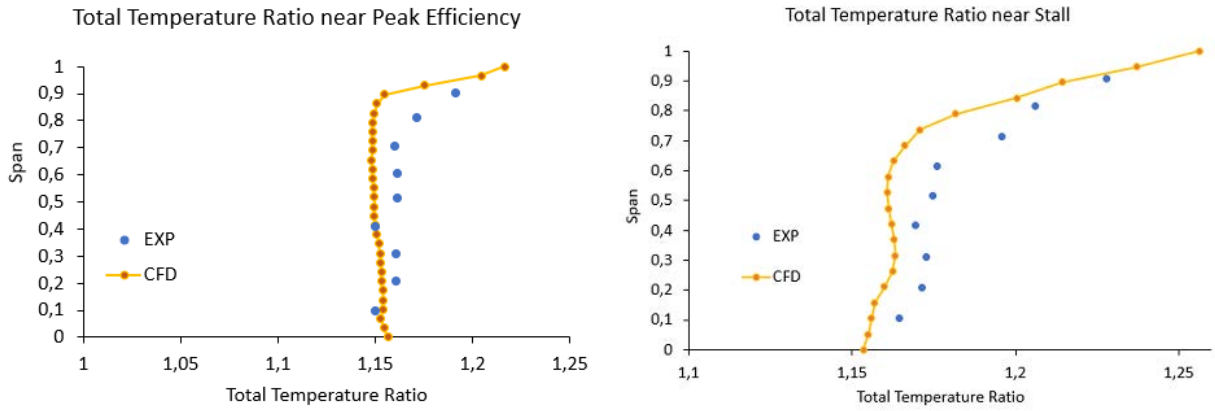

(a) *Total temperature ratio comparison near peak.* **(b)** *Total temperature ratio comparison near stall.*

Figure 2.16: *Total temperature ratios along spanwise direction.*

At station 2 exit flow angles are collected in [6] for peak efficiency and near stall points. Obtained CFD results are shown in Figure 2.18.
Flow motion within a rotor can be expressed in terms of absolute and relative reference frame. The first is fixed while the latter is rotating at the same rotational speed of the rotor.
With reference to the stationary frame, observed velocities are called absolute velocities, while those observed in the rotating frame are called relative velocities. They are linked through the relationship that follows:

$$\vec{c} = \vec{w} + \vec{u} \tag{2.2}$$

- $\vec{c}$ is the absolute velocity
- $\vec{w}$ is the relative velocity
- $\vec{u}$ is the tangential blade speed. $\vec{u} = \vec{\omega} \wedge \vec{r}$

These three speed components form the *velocity triangle*. An example is shown in Figure 2.17.

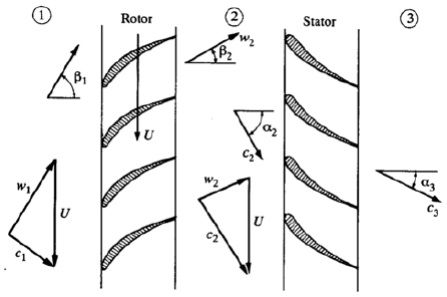

Figure 2.17: *Velocity triangles of an axial compressor.*

For every speed component, it is possible to depict also flow angles with respect to the tangential direction. Those illustrated in Figure 2.18 are referred to absolute velocity component measured at the outlet rotor section.

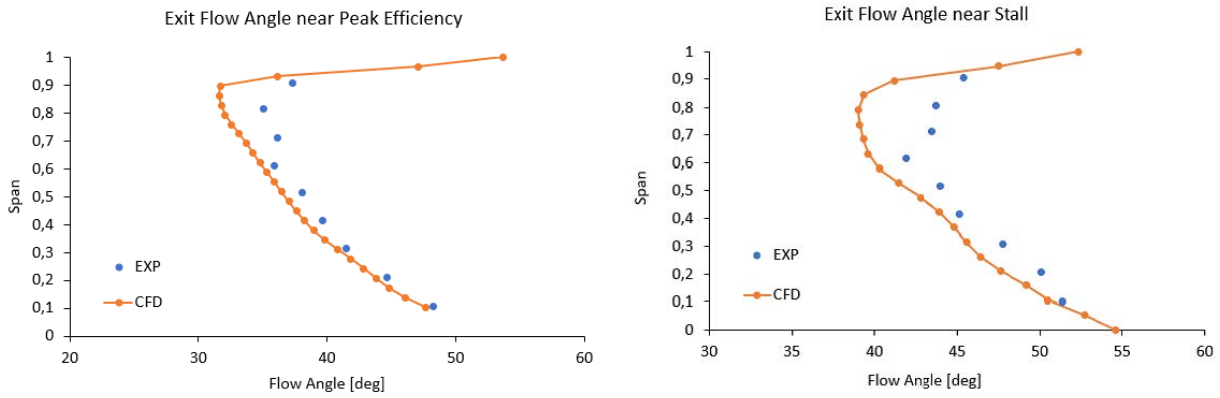

(a) *Exit flow angle at peak efficiency point.* **(b)** *Exit flow angle at near stall condition.*

Figure 2.18: *Exit flow angle vs span normalized of NASA rotor 67.*

Comparison data about Mach number along streamwise direction at 50% pitch and various span values for peak efficiency and near stall conditions are shown:

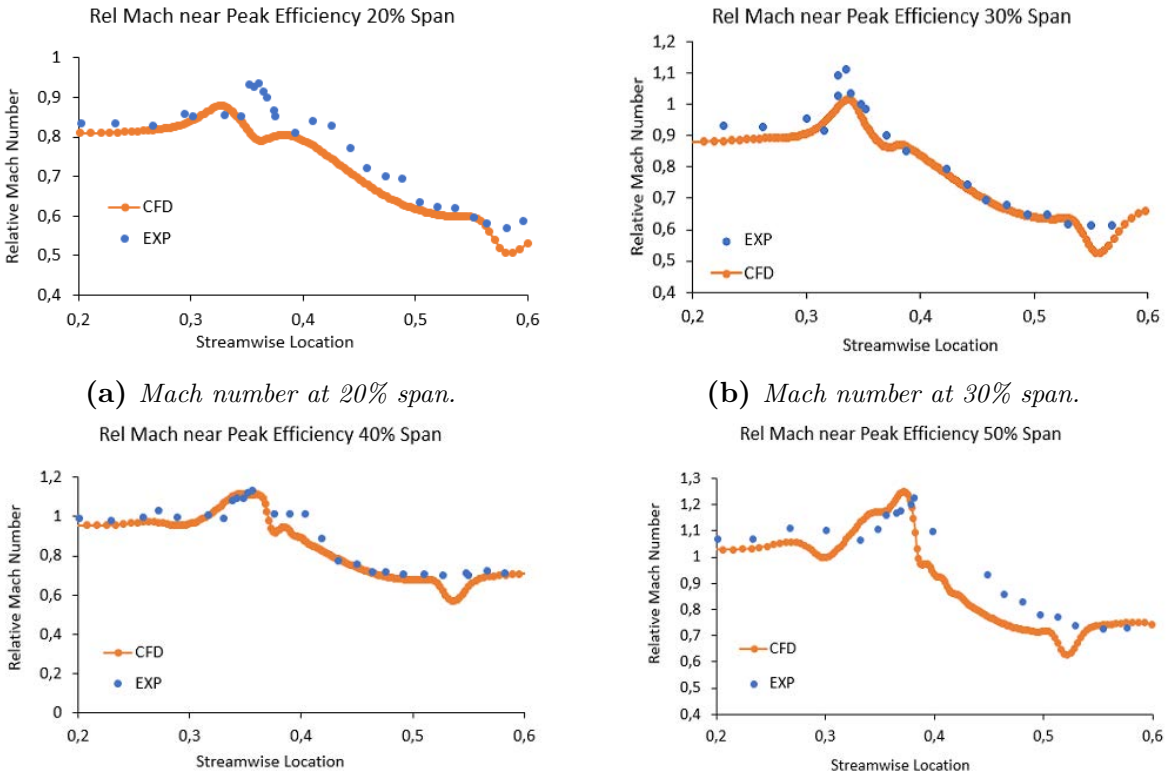

(a) *Mach number at 20% span.* **(b)** *Mach number at 30% span.*

(c) *Mach number at 40% span.* **(d)** *Mach number at 50% span.*

Figure 2.19: *Mach number behaviour at peak efficiency point at 20,30,40,50% span.*

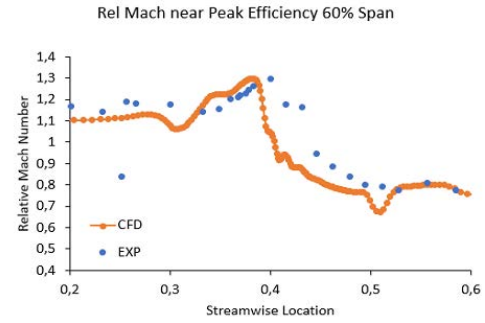

(a) *Mach number at 60% span.*

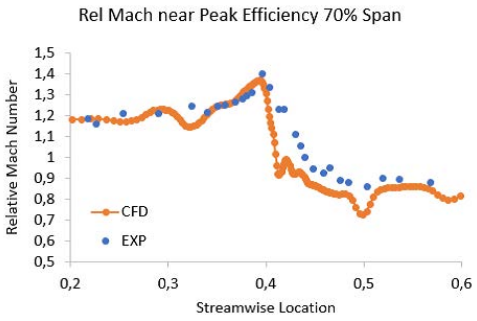

(b) *Mach number at 70% span.*

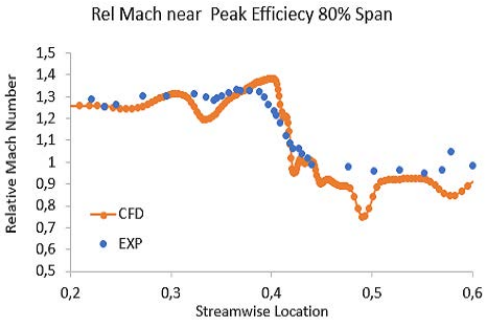

(c) *Mach number at 80% span.*

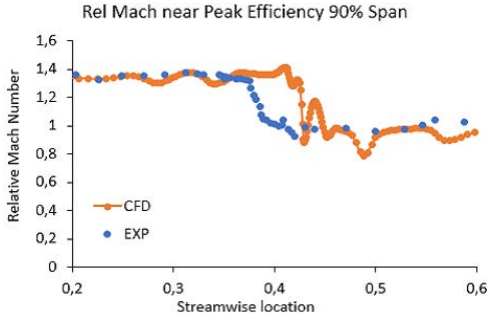

(d) *Mach number at 80% span.*

Figure 2.20: *Mach number behaviour at peak efficiency point at 60,70,80,90% span.*

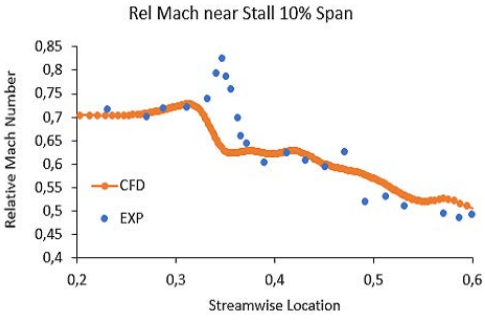

(a) *Mach number at 10% span.*

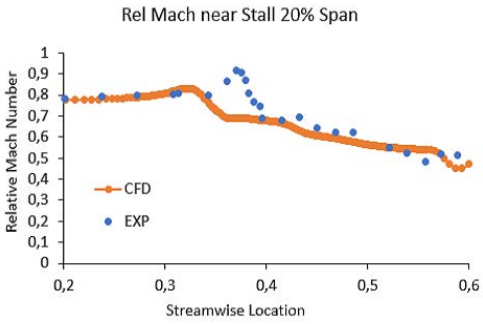

(b) *Mach number at 20% span.*

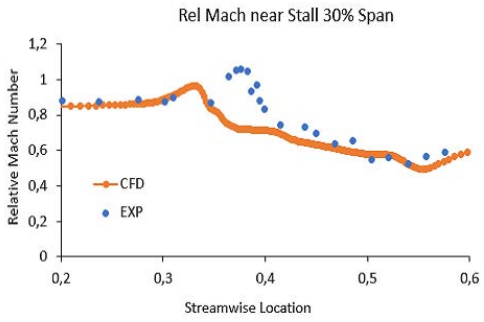

(c) *Mach number at 30% span.*

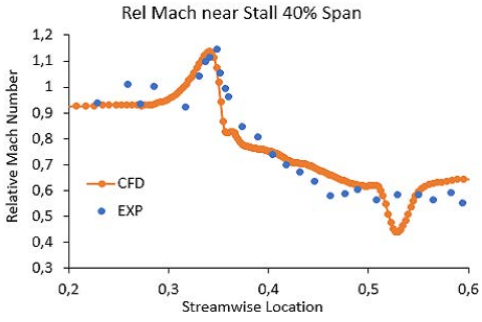

(d) *Mach number at 40% span.*

Figure 2.21: *Mach number behaviour at near stall point at 10,20,30,40% span.*

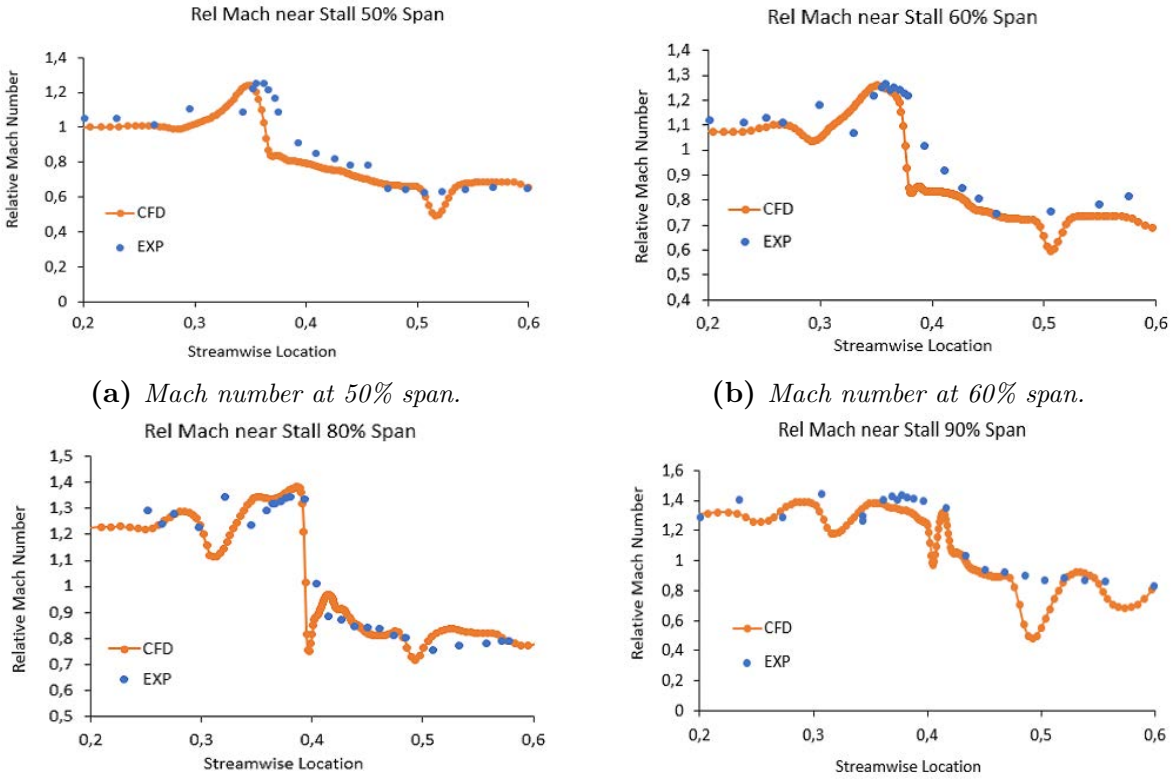

(a) *Mach number at 50% span.*

(b) *Mach number at 60% span.*

(c) *Mach number at 80% span.*

(d) *Mach number at 80% span.*

Figure 2.22: *Mach number behaviour at near stall point at 50,60,80,90% span.*

In Figure 2.23 pressure distribution in streamwise direction is depicted. These images show the consequences of shock waves to pressure trend through pressure side and suction side of the blade. In particular, when span values exceed 50%, along the pressure side there's an increase due to the shock and then a rapid stabilization of pressure, while at suction side, static pressure tends to increase only near the trailing edge because of the shock wave that occurs at the previous blade.
Clearly, since tangential blade speed is proportional to the radius, it increases as a consequence of an increasing radius (i.e. span), therefore shock waves occur from about 50% span because relative Mach number starts exceeding 1.
This fact can be seen also observing Figure 2.9, 2.10, 2.11: at 30% span from hub incoming relative flow is still subsonic but at increasing span values (70% and 90%) relative Mach number reaches 1.35 and shocks at leading edge are clearly visible.

Finally, some contours of Mach number at choking condition are presented (Figure 2.25).
A curious fact can be observed: at choking condition, the shock wave at leading edge is not sufficient to decrease Mach number under unity, indeed another shock in the blade channel is created. This occurs because of a decreasing of static pressure downstream the rotor which causes a flow acceleration after the first shock wave (a weak shock) and another normal shock in the blade channel is formed.
Considering a constant rotational speed, when mass flow decreases (i.e. flow incidence

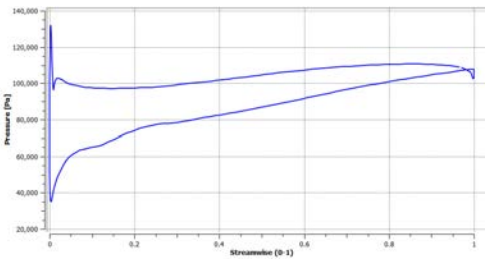

(a) *Pressure distribution at 20% span.*

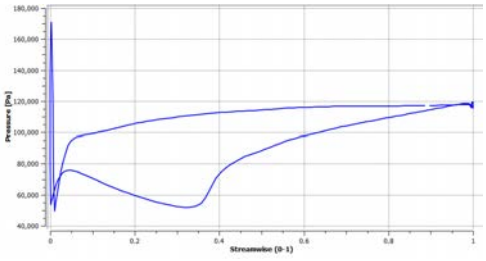

(b) *Pressure distribution at 50% span.*

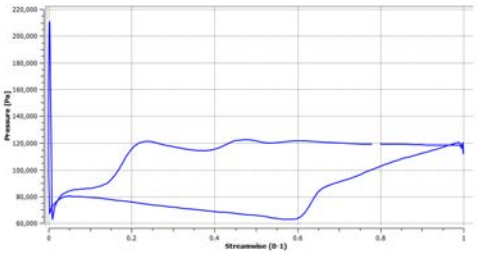

(c) *Pressure distribution at 80% span.*

Figure 2.23: *Pressure loading at different span values at peak efficiency.*

increases), the rotor moves towards near stall condition and at LE the shock becomes detached and normal to the incoming flow [8].

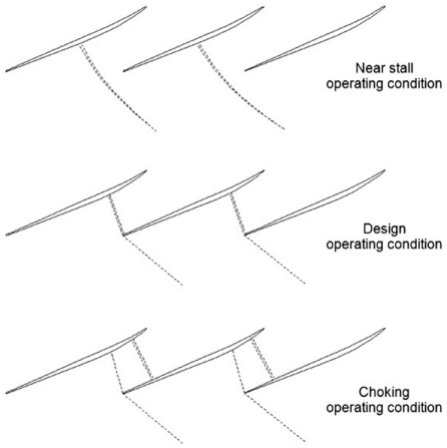

Figure 2.24: *Shock waves configurations in transonic compressor rotor at a constant rotational speed [8].*

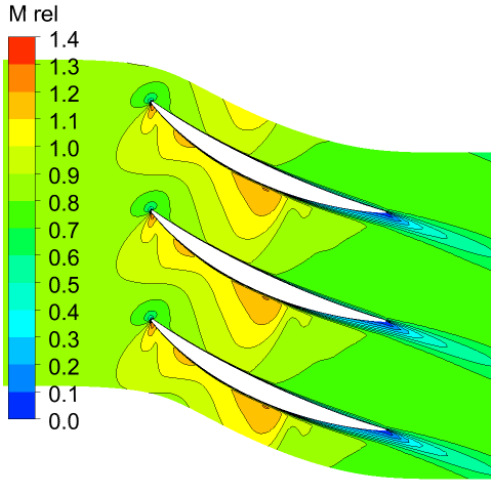

(a) *Relative Mach number at 20% span.*

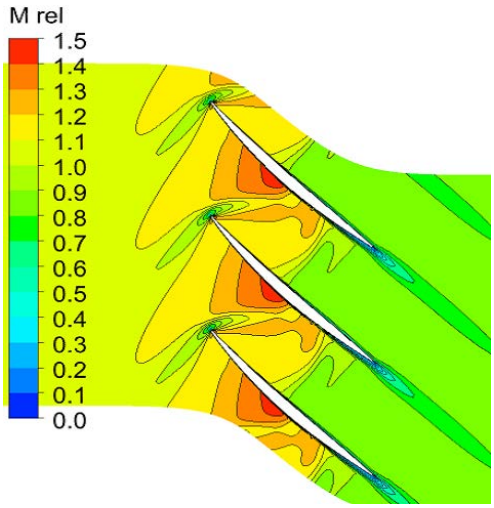

(b) *Relative Mach number at 50% span.*

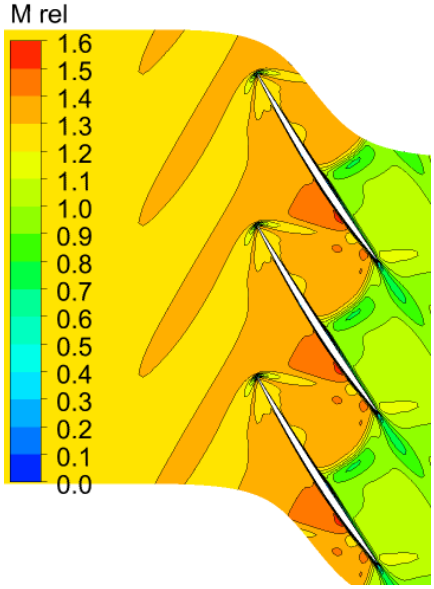

(c) *Relative Mach number at 80% span.*

Figure 2.25: *Blade to blade contours of Mach Rel at some span locations near choke.*

2.4 The Model

As previously said, this section's purpose is to illustrate how the complete model mesh is built, with a particular focus on interfaces and boundary conditions. In this case also, only a single passage is analysed.
In this section the following steps are described:

1. Grid generation description
2. Case setup

2.4.1 Mesh generation

The three principal components are: Rotor 67, spinner and nacelle. Nacelle, spinner, and external flow grid were separately built and then assembled with blade and outlet blocks generated in TurboGrid.
The spinner geometry was made by using Solidworks (Figure 2.26) [21], in particular it has been created with a rotation of a quarter of ellipse of a $\pi/22$ angle in order to create a 3D component. The spinner is characterized by a value of L/D=4.2/5, where L is the length of the ellipse semi-major axis and D/2 is the ellipse semi-minor axis.

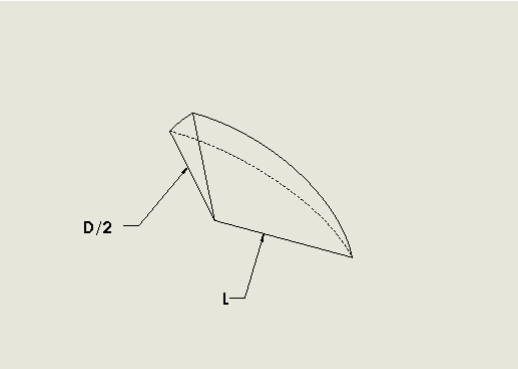

Figure 2.26: *Spinner geometry.*

After importing the spinner geometry, it has been scaled in order to be correctly matched with the fan blade. In particular, since the inlet hub radius of rotor 67 is 9.16 cm, the semi-minor ellipse axis was scaled to that length.

The geometry of the nacelle has been selected from the Nasa common research model which includes also wings, fuselage, pylon and horizontal tail [9]. Originally the model of the entire aircraft focuses on the aerodynamic design of the wing and it has been created to collect detailed aerodynamic performance data, indeed it includes an empty nacelle.

Once imported the nacelle, it also has been conveniently scaled in order to obtain the right configuration of fan single blade (rotor 67), nacelle and ogive. However, before scaling the nacelle component it is very important to determine the right axial position of the

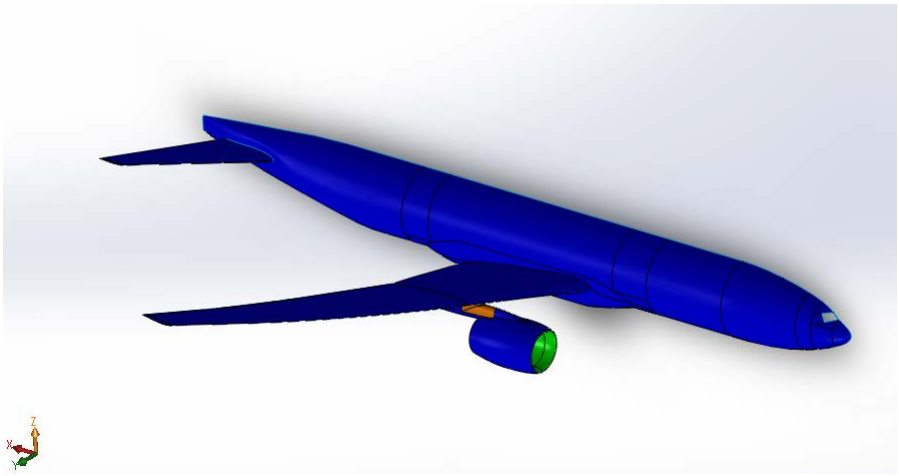

Figure 2.27: *Original reference geometry of the entire aircraft [9].*

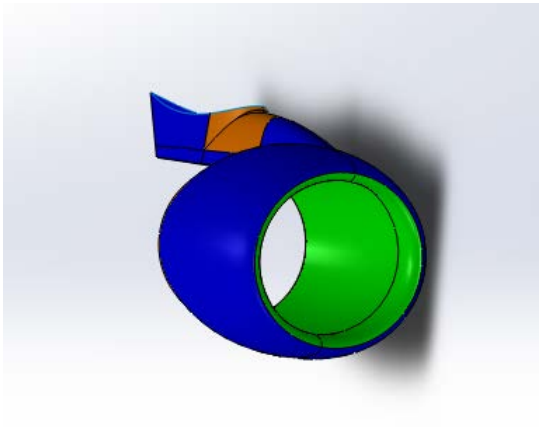

Figure 2.28: *Isolated nacelle and pylon.*

blade in the nacelle and this represents the most important step because it will affect in a significant way all results.
First of all, in the blade positioning process, the following requirements have to be respected in order to obtain a realistic configuration:

1. Freestream Mach number $M_\infty = 0.85$
2. MFCR=0.75
3. The Mach number at fan face (M_{FF}) has to be that obtained from validation study at station 1 (Figure 2.15).

Another known parameter is the highlight section A_i which is measured from the CAD model, consequently also A_∞ is automatically determined.
A Matlab code has been written [22], in this way, using gas dynamics, the correct axial position of the blade can be obtained. In particular, the following relation is the base of the entire method:

$$\frac{A}{A^*} = \frac{1}{M}\left(\frac{1+\frac{k-1}{2}M^2}{\frac{k+1}{2}}\right)^{0.5}\left(\frac{1+\frac{k-1}{2}M^2}{\frac{k+1}{2}}\right)^{\frac{1}{k-1}} \tag{2.3}$$

Where M is the Mach number at a generic section A, A^* is the section where Mach number equals to 1, called *critical section* and k is the ratio between specific heats $c_P/c_v = 1.4$. The code works as follows:

- Step 1: calculation of critical section area
  A^* is determined solving Equation 2.3 in which A and M are replaced by A_∞ and M_∞
- Step 2: fan face area determination
  A^* value obtained in step 1 has been inserted in 2.3 which is solved in terms of fan face area, A_{FF}, replacing M with M_{FF}
- Step 3: Once A_{FF} is known, its radius is calculated:

$$r_{FF} = \sqrt{\frac{A_{FF}}{\pi}} \tag{2.4}$$

- Step 4: obtained radius will correspond to an univocal axial position along nacelle axis. This is therefore the location of fan inlet section.

Since shroud inlet fan height is 25.69 cm, nacelle's scale factor is the ratio between shroud inlet fan radius and fan face radius obtained in step 3.
Referring to Figure 1.13, a way to verify the right position is the obtained nacelle L/D measurement. As previously said, traditional L/D values are about 0.5 and the obtained one is L/D=0.47.
Finally the nacelle profile has been rotated of a $\pi/22$ angle too.

The target is to build a completely structured mesh and both spinner and nacelle surface meshes are characterized by 3168 and 9312 quad elements respectively (Figure 2.29); a structured grid is composed by only hex elements representing an appropriate method for CFD analysis. The main drawback is the fact that it takes a huge amount of time because of the lack of automatic procedures to generate structured grids able to guarantee good quality for complex geometries.
For the boundary layer mesh, near solid surfaces, the need to tighten grid points in the direction normal to the surface is motivated by the requirement to capture flow details due to large gradients of physical quantities, therefore it is essential to quantify first cell height by the assessment of Reynolds number calculated imposing freestream velocity, reference length (in this case nacelle scaled highlight diameter) and the desired y+ value as 1. Since freestream Mach number, total pressure and total temperature are known, freestream velocity V_∞ is found using isentropic relationships (to obtain static pressure and temperature) and Mach number definition:

$$\frac{T^0}{T} = 1 + \frac{k-1}{2} M_\infty^2 \tag{2.5}$$

$$\frac{p^0}{p} = \left(1 + \frac{k-1}{2} M_\infty^2\right)^{\frac{k}{k-1}} \tag{2.6}$$

$$V_\infty = M_\infty \cdot a = M_\infty \cdot \sqrt{kRT} \tag{2.7}$$

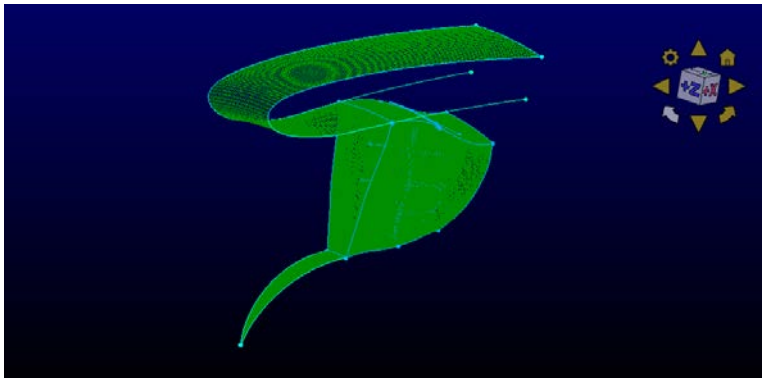

Figure 2.29: *Spinner, nacelle and blade structured mesh.*

In Equation 2.7, a is the local speed of sound and R=287.05 J/(kgK) the gas constant. Reynolds number resulted $5.4 \cdot 10^6$, the first cell height $\Delta s = 10^{-6}$ m [23] and the imposed cell growth rate was 1.1 for a total of 40 layers. Within the entire domain, the y+ value does not exceed 40; in particular the maximum y+ value of 31 is obtained at blade tip because during mesh construction for the validation analysis, first cell height was slightly greater than that obtained for the entire model (Figure 2.30).
The domain extends to $15r_i$ (highlight radius) in z direction starting from spinner's end and $10r_i$ in y direction starting from outer nacelle surface. As a result, the final mesh is a multi-block totally structured grid with a total of 5.5M elements.
This mesh is a result of a compromise between a good quality grid and an adequate number of cells to obtain an acceptable calculation time.

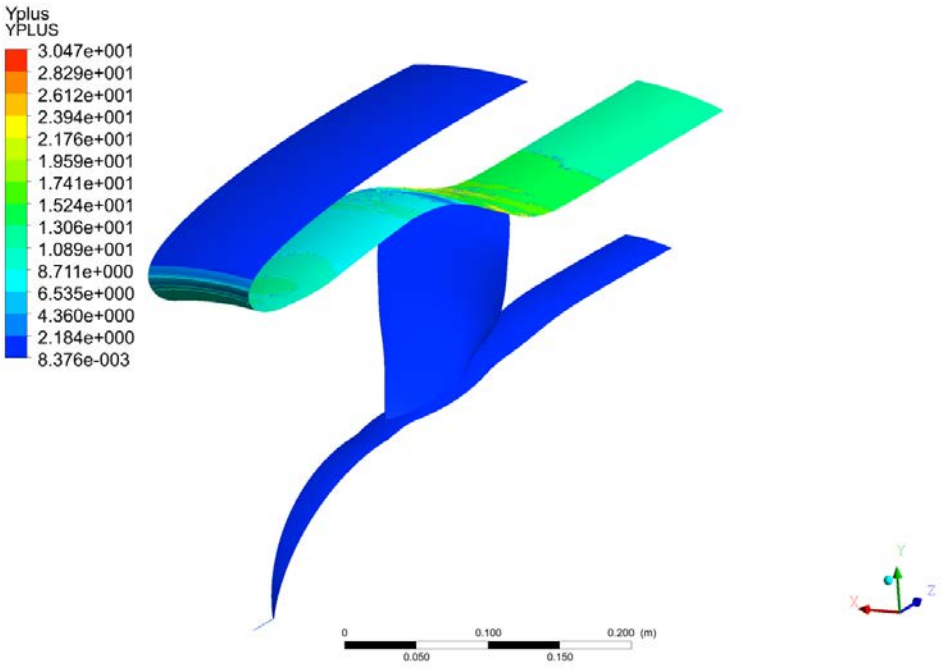

Figure 2.30: *Obtained y+ contours.*

2.4.2 Case setup

CFD model was created using CFX-Pre in which six principal blocks were imported in .cgns format:

- Block 1: Rotor 67 blade
- Block 2: Blade outlet
- Block 3: Nacelle's boundary layer grid
- Block 4: Spinner's boundary layer grid
- Block 5: Nacelle inlet (that is the grid part from throat section to fan face included in boundary layers explained above)
- Block 6: Farfield, which includes all remaining elements

The main parameters were set in the same way as made during validation. The calculation is steady state and for turbulence the $k - \omega - SST$ model is used. High resolution for turbulence and advection scheme is set.
All blocks except the first two were imposed as stationary; blade, outlet blocks and spinner surface are rotating with the 100% fan rotational speed of 16043 RPM. Despite in reality outlet block is stationary, it has been set as rotating in order to avoid reverse flows near outlet boundary condition which will considerably affect the solution because in these cases the solver places a wall to prevent the flow to change direction.

2.4.3 Interfaces

In this model a correct interfaces setting is essential to achieve good results. Normally, CFX-Pre oversees in automatic interfaces setting but in the considered setup case, mesh interfaces have to be manually created. The two sides of the domain were connected through rotational periodicity in which z-axis has been specified from axis definition area and for internal connection between the blocks interface type was set as fluid-fluid with a general connection for interface model.
Since the flow has to travel from a stationary frame (from inlet to fan face) to a rotating frame (from fan face to outlet), the stage mixing plane interface is needed [24]. In this way, as the flow crosses the interface, the solver circumferentially averages fluid's information in terms of total pressure or velocity converting it in inlet condition for next reference frame. In the specific analysed case, average velocity is selected, therefore the rotor sees it as an inlet condition.

2.4.4 Boundary Conditions

As for the validation study, to set inlet conditions, total pressure and total temperature of 101325 Pa and 288.2 K respectively were selected. In a different way outlet conditions are

treated because there is the need to define two separate outlet conditions (see Figure 2.31). In both cases average static pressure option is selected but for nacelle's external flow, static pressure was calculated from total pressure and freestream Mach number using Equation 2.6, while for blade outlet, static pressure has been modified for every simulation in order to describe rotor performances from choking to near stall condition obtaining its speedline.
Blade shroud was set as counter rotating wall and the farfield boundary as free slip wall [25].

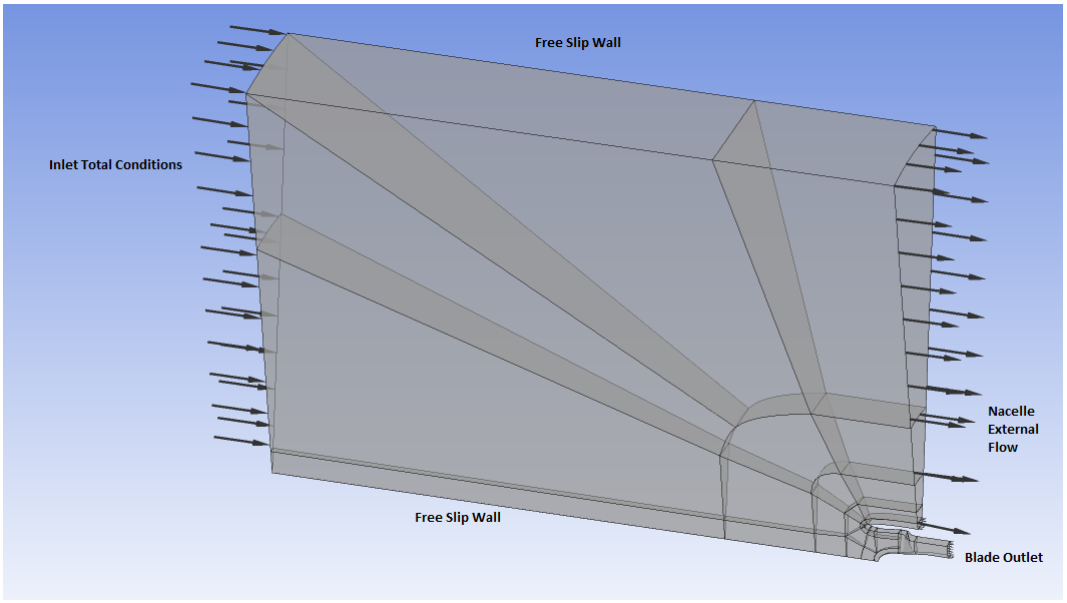

Figure 2.31: *Single passage and boundary conditions in CFX-Pre.*

- III -

Results and Discussion

Blade, spinner and nacelle interaction was simulated using computational fluid dynamics to verify the correct installation of the blade and the influence exerted by the insertion of the ogive and intake added to the single rotor blade. Since the model represents an axisymmetric case, all simulations are characterized by a AoA=0° neglecting also installation highlight section angle.
Since there are not experimental data available for validation, the present chapter discusses the obtained results.
The following table summarizes first simulations main parameters:

Inlet total pressure [Pa]	101325
Inlet total temperature [K]	288.2
Blade rotational speed [RPM]	16043
Spinner rotational speed [RPM]	16043
Freestream Mach number [-]	0.85
Freestream velocity [m/s]	269.43
Blade outlet static pressure [Pa]	variable
External flow static pressure [Pa]	63177.34
AoA [deg]	0

Table 3.1: *Imposed parameters for the first case study.*

The second part of the present chapter will consider a different flight condition, in particular, obtained data from other simulations will be analysed, in which different boundary conditions with respect from those considered previously were set. These last were imposed so as to achieve a freestream Mach number of 0.2.
More specifically, the choice was to mantain an inlet total pressure and total temperature of 101325 Pa and 288.2 K respectively, while the only modified BC is the nacelle external flow outlet condition. In that sense, the appropriate average static pressure value was evaluated from isentropic relationship (Equation 2.6) that links the ratio between static and total pressures with the Mach number, resulting in 98518 Pa.
Second simulation's data are collected in the following table:

Inlet total pressure [Pa]	101325
Inlet total temperature [K]	288.2
Blade rotational speed [RPM]	16043
Spinner rotational speed [RPM]	16043
Freestream Mach number [-]	0.2
Freestream velocity [m/s]	67.79
Blade outlet static pressure [Pa]	114500
External flow static pressure [Pa]	98518.2
AoA [deg]	0

Table 3.2: *Imposed parameters for the second case study.*

3.1 Characteristic maps

In this section, compressor maps are illustrated; some differences from those achieved during single channel validation are expected, in particular a decrease in isentropic effciency is shown, while for total pressure ratio those differences are not quite evident.

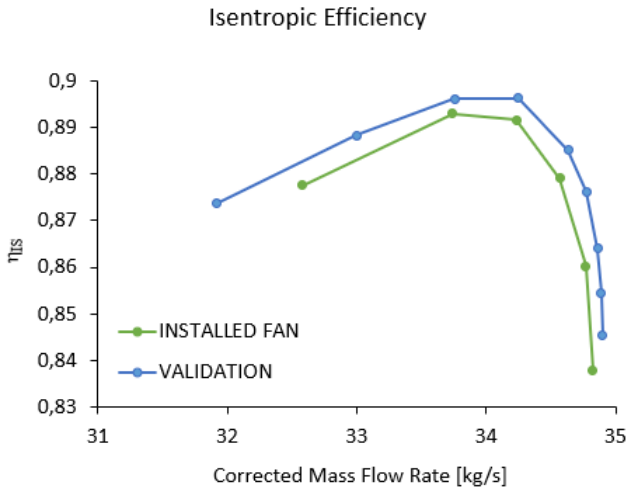

Figure 3.1: *Isentropic efficiency comparison among installed fan and single channel simulation.*

As to better notice the differences in terms of mass flow rate, the following plots don't present the normalized mass flow rate in x-axis, but for each curve point the corrected mass flow rate is computed as explained in Equation 1.23, in which p_1^0 and T_1^0 are extracted from the post processing at fan face section.
As a matter of fact, corrected mass flow rate at choking is slightly lower for the installed rotor, decreasing of 0.22% with respect to the validation case, which corresponds to a difference of $\Delta\dot{m}_{c,choke} = 0.077$ kg/s. From isentropic efficiency perspective, the integration of the blade in the intake causes a reduction in rotor performances and a relocation of the peak efficiency point from $\dot{m}_c = 34.2501$ kg/s for the validation analysis to $\dot{m}_c = 33.74276$ kg/s for the installation case, which were found at a blade average outlet static pressure

of 114500 Pa and 118000 Pa respectively. Peak efficiency resulted in $\eta_{is,installed}^{peak} = 0.893$ with a decrease of 0.37% from the value of $\eta_{is,validation}^{peak} = 0.896$.
Total pressure ratio for each speedline point is computed as the ratio between total pressure at blade outlet and total pressure at fan face, resulting in a very similar trend for both curves.

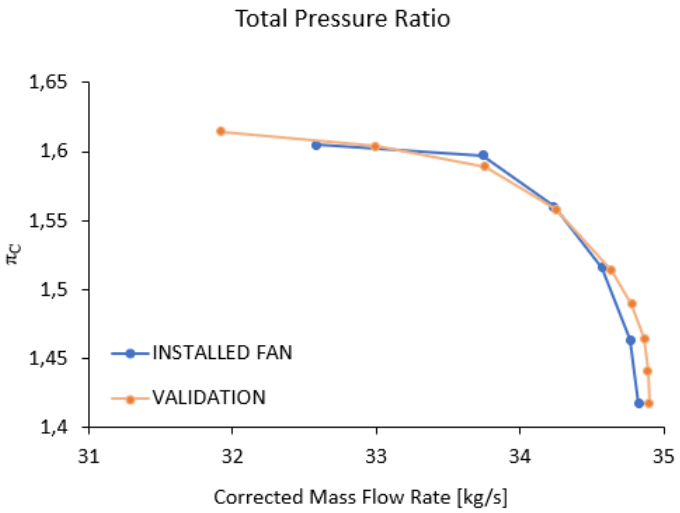

Figure 3.2: *Total pressure ratio characteristic map comparison.*

It can be seen that, the installation of the blade coupled with the rotating spinner inside the intake, has little influence on rotor performances in terms of fluid's compression capability; even there is a spot where the installed fan seems to work better when coupled with ogive and nacelle.
The differences highlighted between the two models, however small, are caused by the adoption of a different model.

	Validation	Installed	Δ
$\dot{m}_{c,choke}$ [kg/s]	34.9015	34.82415	+7.735e-02
Blade outlet 114500 Pa			
$\dot{m}_c$ [kg/s]	34.2501	34.23315	+1.695e-02
π_C	1.5583	1.56032	-0.202e-02
η_{is}	0.896261	0.891692	+4.569e-02
Blade outlet 118000 Pa			
$\dot{m}_c$ [kg/s]	33.7565	33.74276	+1.374e-02
π_C	1.5892	1.59712	-0.792e-02
η_{is}	0.896147	0.892974	+0.317e-02

Table 3.3: *Single blade and installed blade simulations' comparison*

Referring to Table 3.3, last column's values are the difference between validation and installed case of the first column's quantities.

3.2 Intake Evaluation

Once the fluid is captured in the nacelle, it passes through the intake before encountering the fan. The role of an air intake is to capture the airflow needed by the propulsor for every flight condition in order to provide the maximum thrust and the minimum drag [26]. For subsonic flights, intake is in general a convergent-divergent duct designed properly to diffuse the incoming stream of fluid and to reduce inlet airflow distortions [27]; its total pressure ratio is defined as:

$$\pi_D = \frac{p_1^0}{p_{amb}^0} \tag{3.1}$$

where the subscripts 1 refers to fan face section and amb refers to ambient condition, i. e. the total pressure of the freestream. Another way to judge subsonic intake's performances is the diffusion isentropic efficiency:

$$\eta_D = \frac{T_{1,is}^0 - T_{amb}}{T_1^0 - T_{amb}} = \frac{(p_1^0/p_{amb})^{\frac{k-1}{k}} - 1}{\frac{k-1}{2} M_\infty^2} \tag{3.2}$$

Both parameters are influenced by the flight Mach number: they both decrease as the freestream Mach number increases.
Next table presents a summary of intake total pressure ratio and isentropic efficiency near stall, near peak efficiency and near choke:

Condition	π_D	η_D
Near choke	0.996	0.991
Near peak	0.9966	0.992
Near stall	0.9965	0.992

Table 3.4: *Intake performances at some rotor conditions.*

Results contained in the previous table confirm what previously declared or rather that diffusion isentropic efficiency depends on Mach number. This is proved also by Equation 3.2, which is function only of Mach number, total and static pressure upstream the intake; indeed both π_D and η_D present negligible changes when rotor conditions vary. Since rotor conditions variation means different blade outlet conditions, the same conclusion could be done about intake's total pressure ratio because of its dependence only on total pressures upstream the fan, i. e. it depends on Mach number.

3.3 Streamtubes and Mach Number Distribution

As introduced in the first chapter, the main purpose of this work is to study and analyse how the match of a fan blade with the intake and the spinner works. A preliminary assessment consists on the pre-entry streamtube's shape evaluation, in other words, to take into consideration the MFCR; speaking of the mass flow capture ratio, three configurations exist: MFCR=1, MFCR<1 and MFCR>1.

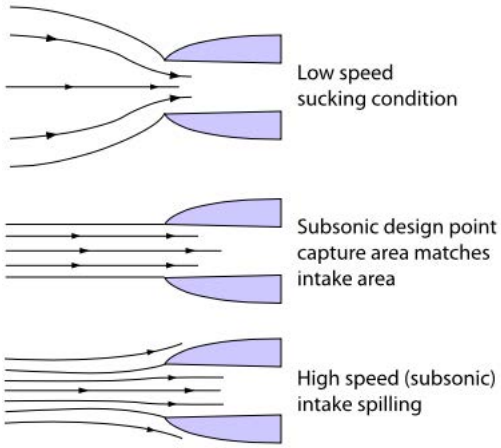

Figure 3.3: *Pre-entry streamtube shapes. Starting from the top: MFCR>1, MFCR=1, MFCR<1.*

- MFCR>1: sucking condition. This situation tipically occurs when low speeds are considered, especially during take-off phase. In this case, the incoming airflow, tends to accelerate right upstream the propulsor.
- MFCR=1: cylindrical inlet flow. The airflow velocity remains constant in the pre-entry streamtube and this represents the optimal or design point
- MFCR<1: intake spilling. This occurs when the freestream Mach number reaches transonic values and the airflow tends to get slower before entering in the intake.

Since first simulations' inlet conditions were set in order to obtain $M_\infty = 0.85$, a MFCR<1 is expected, obtaining $A_\infty < A_i$.
Figure 3.4 shows the obtained streamtube entering the propulsor, in which a MFCR<1 is clearly visible, in particular the obtained MFCR value is $A_\infty/A_i = 0.6$.
Moreover, the airflow withstands an huge deceleration quantifiable from the comparison between the Mach at highlight section and the freestream Mach number for the three principal rotor conditions:

Condition	M_i/M_∞
Near choke	0.58
Near peak	0.55
Near stall	0.54

Table 3.5: *Mach number reduction from capture to highlight section.*

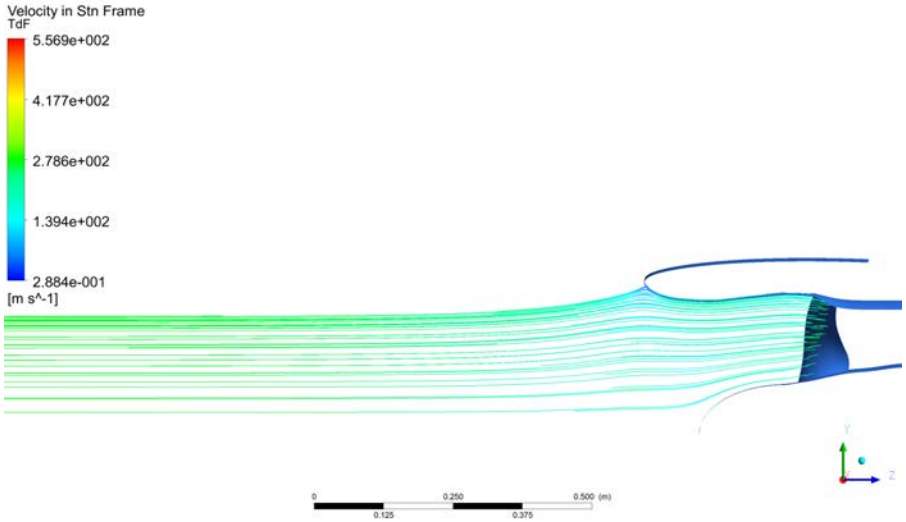

Figure 3.4: *Pre-entry obtained streamtube.*

From the cylindrical inlet flow condition, intake spilling one presents a difference in terms of stagnation point location, indeed it shifts from highlight section (for MFCR=1) towards the throat causing, as previously explained, the air to move around the nacelle's lip to the external surface because the stagnation point indicates the point, with zero speed value, where the incoming airflow divides into internal and external flow.

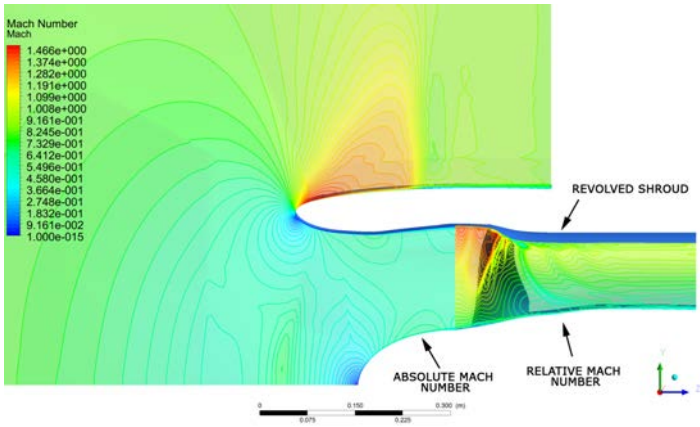

Figure 3.5: *Mach number distribution around nacelle's surface and through the intake. The blue surface located over the blade and the outlet block represents a portion of the shroud which has been rovolved around propulsor's axis.*

From Figure 3.5, the fidelty of the achieved data with theoretical aspects comes to light, as a matter of fact, Mach number distribution on nacelle's external surface follows the expectations put in light when talking about wave drag and critical Mach number. In particular, from stagnation point towards outside, the flow is subjected to an acceleration from a zero Mach number to M=1 around nacelle's lip, up to a supersonic region in which Mach number reaches its maximum value of 1.47; this flow field portion ends with a shock wave leading again the airflow to a subsonic speed.

3.3.1 Blade to Blade Mach number

In this section some considerations about the Mach number distribution around the blade and in the blade channel are made, as to correctly evaluate which the main installation effects on the fan are.
The chapter validating the CFD model highlighted the consequences that the different rotor operating conditions (stall, peak efficiency, and chocking) would have on the distribution of Mach number around the blade and inside the blade channel. It was in fact seen that, from blade's certain span onwards, the relative velocity of the flow exceeds the local speed of sound, thus creating shock waves near the leading edge. These shocks can be attached or detached from the body, depending on the blade's condition. It has been seen how the results obtained from the simulation in which the fan was not installed in the intake, aligned with the expectations provided by the theoretical studies. When, on the other hand, the coupling between Rotor 67, ogive, and nacelle is considered, their mutual influence translates into some differences in terms of Mach number and positioning of the shock wave.

The near peak efficiency operating condition of the installed configuration (Figure 3.6) presents an incoming airflow's relative velocity slightly greater than that resulted during validation process, this means that the intake tends to give to the relative flow an acceleration. At 30% span, the difference in incoming flow's relative Mach number is about $\Delta M_{rel} = 0.1$, since for the uninstalled blade $M_{1,rel} \cong 0.85$ while for the installed one $M_{1,rel} \cong 0.95$. Moreover, a more evident discrepancy between the two cases is shown at blade outlet, in which $\Delta M_{rel} \cong 0.5$, therefore the coupled blade is able to provide a major slowing down of the relative stream.
The same conclusions can be made at 70% span from hub, while at 90% span the two configurations present similar characteristics, except for the shock wave at leading edge, which tends to have a slight detachment in the second case of installed fan.
However, the same physical flow features are observed: in both cases, at low span values, the adverse pressure gradient in streamwise direction causes an acceleration and the appearance of a sonic bubble at pressure side, within that the Mach number exceeds unity.

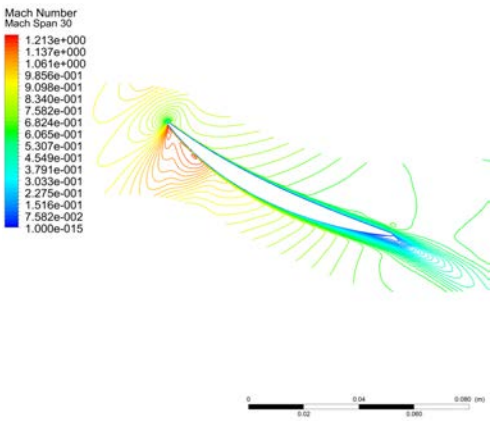

(a) *Relative Mach number at 30% span.*

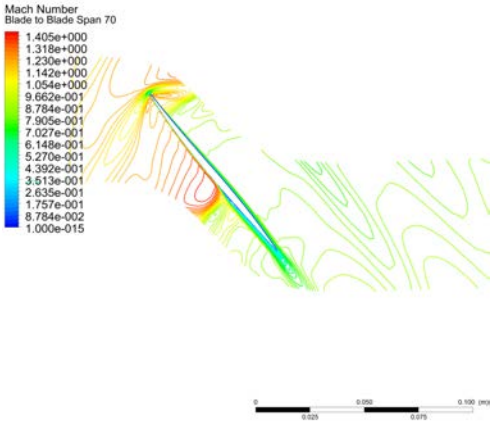

(b) *Relative Mach number at 70% span.*

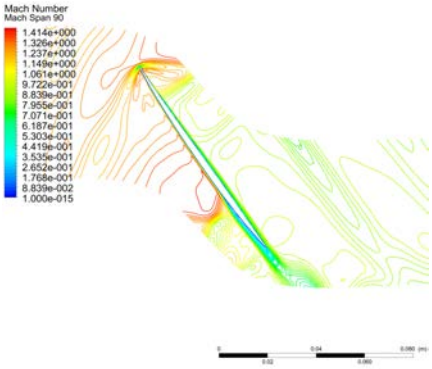

(c) *Relative Mach number at 90% span.*

Figure 3.6: *Blade to blade contours of relative Mach number in the installed fan configuration near peak efficiency.*

Also near stall condition, at 30% and 70% span the relative Mach number upstream the fan is slightly greater for the installed blade and in corrispondence with the airfoil back end, the deceleration is more evident.
Shock waves are now detached from the leading edge as happened for the uninstalled case, but this detachment is exacerbated for the second model. As in validation, the shock is normal to flow direction, leading the airflow to a subsonic speed with no further shocks along the channel; on the pressure side, the shock wave coming from the previous blade is visible and it contributes in decreasing the supersonic Mach number in the sonic bubble. In Figure 3.7, because of the huge shock detachment, Mach number contours of 50% blade span are reported too.

Examining the Mach number distribution for the choking condition presented in Figure 3.8, in this case also the trend highlighted before about the incoming stream persists, in fact there is an increment in terms of relative Mach number of about $\Delta M_{rel} = 0.1$ at 20% span from hub, while at 50% this augmentation decreases up to $\Delta M_{rel} = 0.07$. At 80% span the difference in Mach values is negligible.
Shock waves occurs from mid-span onwards, but traveling along the channel, the fluid is subjected to another shock because of the inability of the first shock, located at LE, to make the flow subsonic. At 80% span, the shock wave's incidence angle has increased if compared to Figure 2.25 (c), at 90% span this incidence is lightly enlarged.

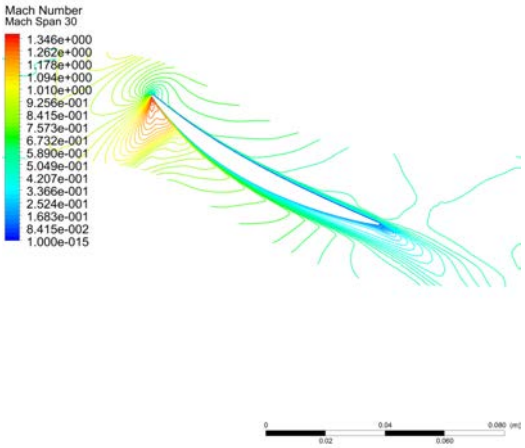

(a) *Relative Mach number at 30% span.*

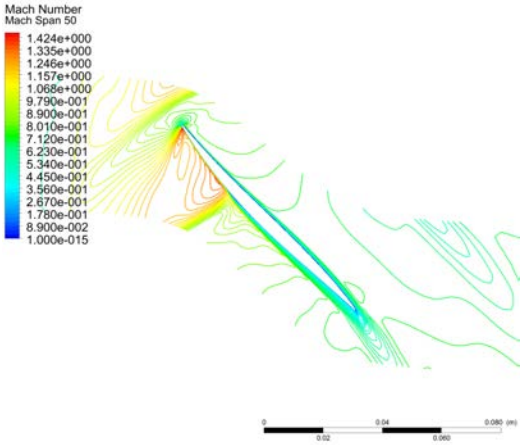

(b) *Relative Mach number at 50% span.*

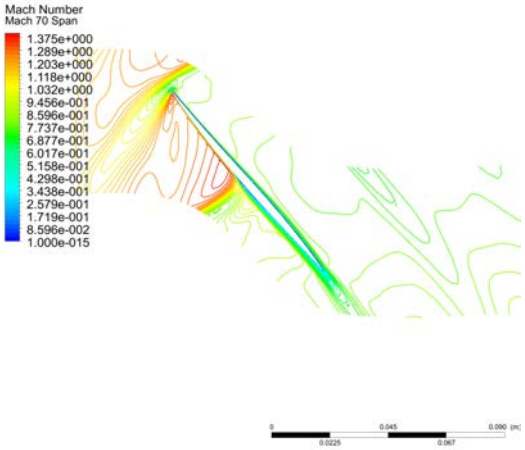

(c) *Relative Mach number at 70% span.*

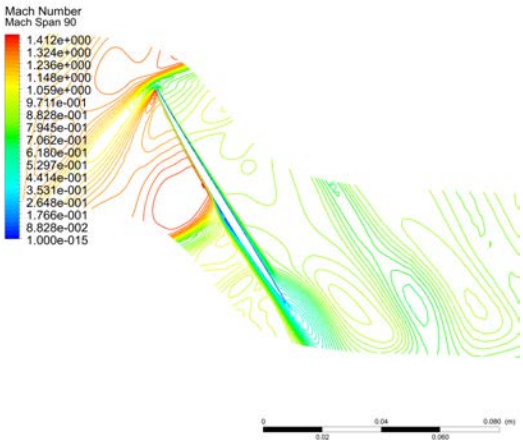

(d) *Relative Mach number at 90% span.*

Figure 3.7: *Blade to blade contours of relative Mach number in the installed fan configuration near stall.*

From previous considerations, it's immediate to deduce that the intake's insertion upstream the compressor entails a little total pressure's decline as compared to the freestream, leading the flow no more isentropic.
Moreover, the correct installation is highlighted by three principal reasons:

1. Since, because of simulation's stability, the choice was to impose total pressure and total temperature as inlet boundary conditions, the average static pressure of the freestream (from the external nacelle's surface onwards) has been calculated in order to obtain $M_\infty = 0.85$. The achieved freestream Mach number (that deducted in the post-processing phase), presents a maximum relative percentage error of 1.5% depending on the point on the fan characteristic map which is located.

2. The second requirement estabilished that $M_{FF} = 0.53$. In this case also, the committed error resulted in a reasonable value of 5.5%

3. The obtained intake's L/D ratio resulted as a consistent value if compared to the expectations, as to indicate the validity of the MATLAB code which was created specifically to correctly locate the rotor on the nacelle's axis.

However, the requirement on the mass flow capture ratio has not been achieved, seeing as a MFCR=0.58 is obtained, while the target value was 0.75. The reason of this discrepancy is supposed to be due to the fact that, during the model assembly, the mass conservation equation has not been taken into account.
With regard to the Mach number distribution, obtained data can't be validated because of the lack of experimental data, neverthless they completely reproduce theoretical considerations.
Focusing instead on blade to blade Mach number, installation results can be compared to the validation ones, which comparison allows to affirm that the installation doesn't cause differences in terms of phenomenon's physics, but it alters only the detail.

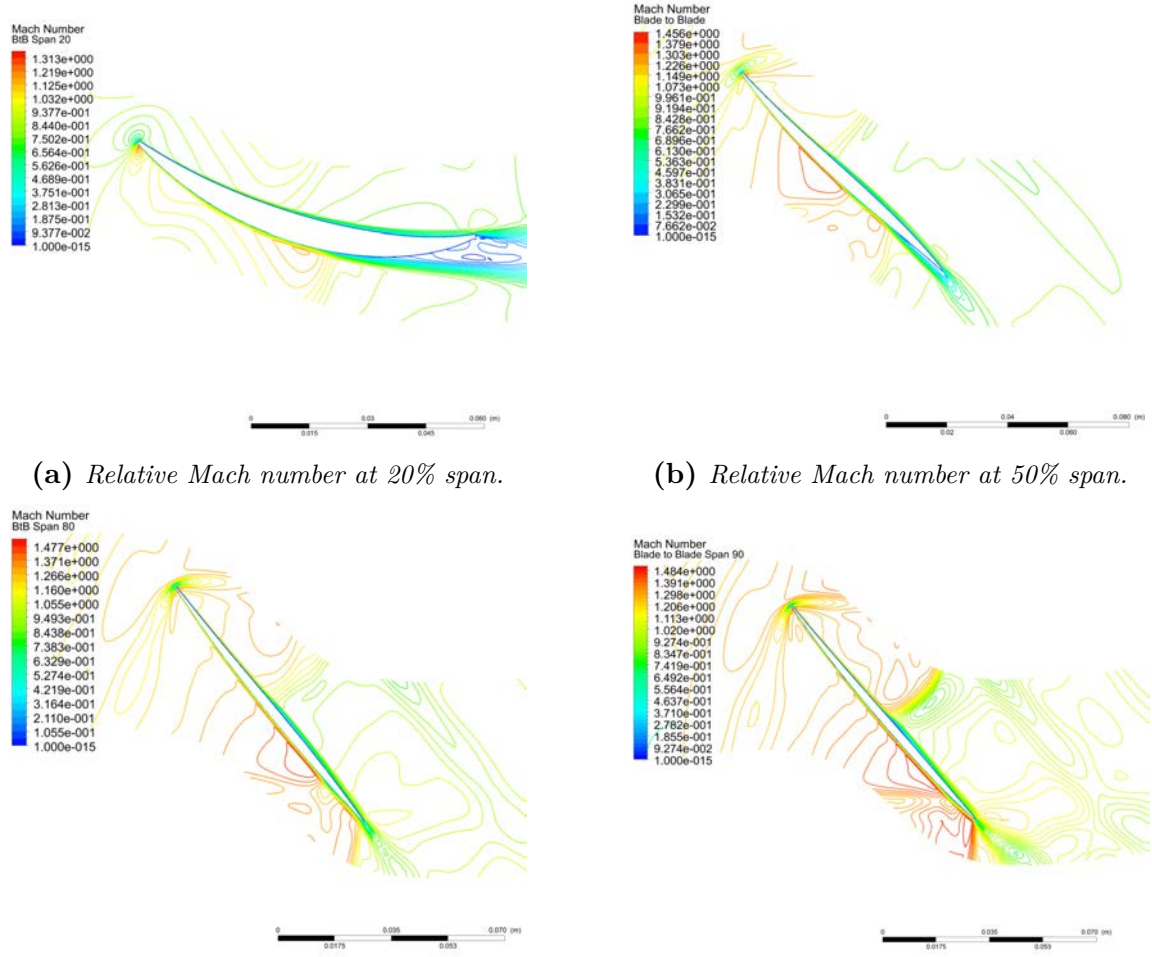

(a) *Relative Mach number at 20% span.*

(b) *Relative Mach number at 50% span.*

(c) *Relative Mach number at 80% span.*

(d) *Relative Mach number at 90% span.*

Figure 3.8: *Blade to blade contours of relative Mach number in the installed fan configuration at choking condition.*

3.4 Second Case Study

At the beginning of the present chapter, the second test case's imposed parameters were introduced. In particular, the setting of a different outlet BC for the freestream over the nacelle's external surface, permits to obtain a freestream Mach number of 0.2.
Even though, because of the zero AoA, this situation could not represent any realistic flight condition, in this way, the goal with this simulation, is to have a situation attributable to the take-off one.
The entire compressor map has not been completed, but in this case only the near peak efficiency point has been extracted. The following plots present the three configurations in comparison (validation, $M_\infty = 0.85$ and $M_\infty = 0.2$) in terms of characteristic maps:

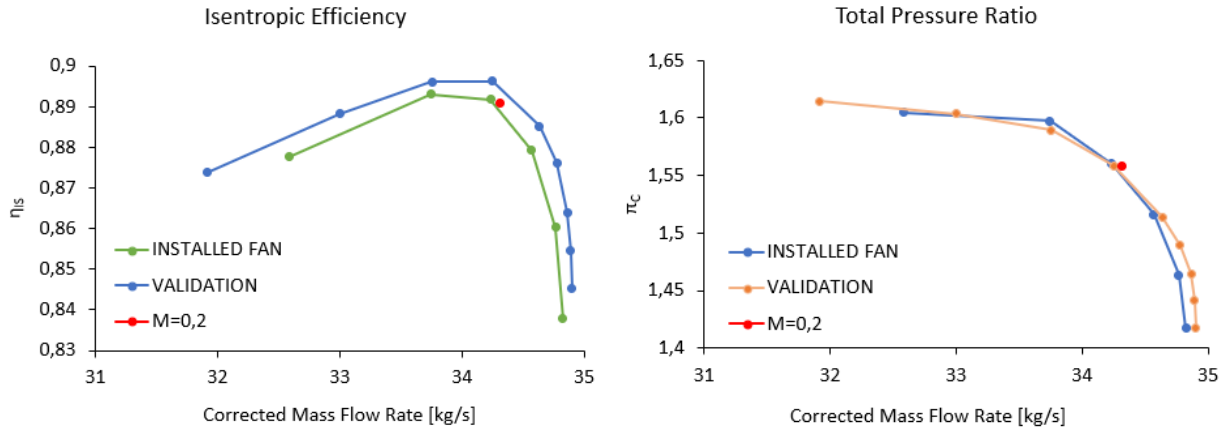

(a) *Isentropic efficiency.* **(b)** *Total pressure ratio.*

Figure 3.9: *Characteristic compressor maps comparison of the three cases.*

As it has been described earlier, the speedline is obtained changing, for every simulation, the average static blade outlet pressure, and for the red point in Figure 3.9 an outlet static pressure of 114500 Pa has been set.
The similarity between the same point of these three cases is very encouraging, since the installed fan's results present the same trend if compared to the single channel outcomes.
In Table 3.6 the main parameters are collected, in addition, in the last column, the difference of the second case study from the uninstalled blade is pointed out.

	Single channel	$M_\infty = 0.85$	$M_\infty = 0.2$	Δ
$\dot{m}_c$ [kg/s]	34.2501	34.23315	34.31421	+6.411e-02
η_{is}	0.896261	0.891692	0.8908	-0.5461e-02
π_C	1.5583	1.56032	1.558	-0.03e-02

Table 3.6: *Single blade vs installed cases near peak efficiency.*

To verify the correct installation, the main preliminary aspect to consider is the pre-entry streamtube shape, since, referring to Figure 3.3, at low speed the streamtube has a convergent shape through the highlight section, presenting a sucking condition, in which $A_\infty > A_i$ and the flow accelerates in correspondence with the inlet section.
This situation generally occurs at take-off phase, when the fan is rotating at its maximum rotational speed and the engine works near to its maximum power.
The second simulation's obtained streamtube sure enough results consistent with the expectations, presenting a convergent shape as to affirm the validity of the model.

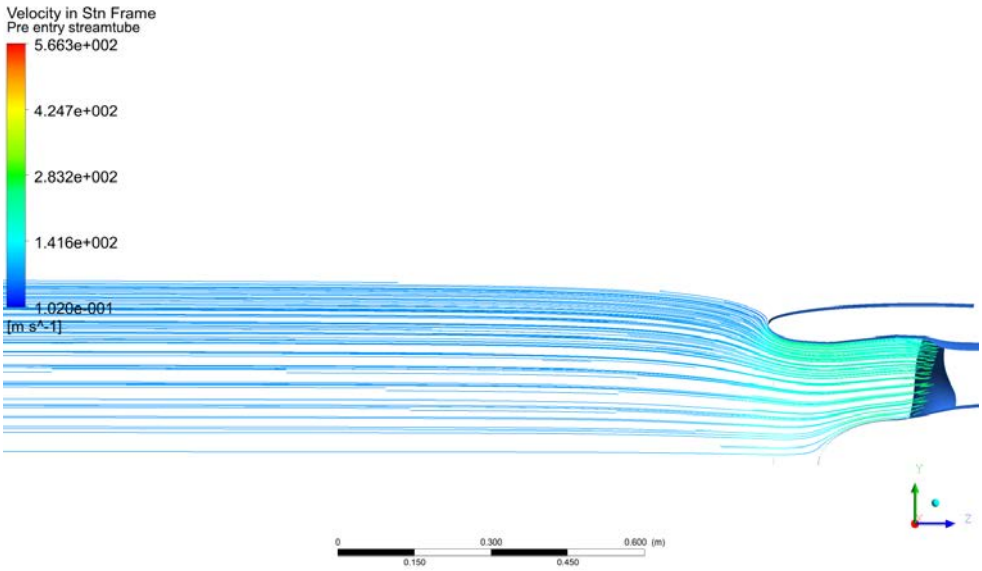

Figure 3.10: *Pre-entry streamtube for the $M_\infty = 0.2$ simulation.*

Comparing Figure 3.10 with Figure 3.4, the different condition of the streamtube entering the propulsor is due to the relocation of the stagnation point, which in the second case study, moves outward, positioning on the outer nacelle's surface. Thus the flow has to travel around the lip towards the inlet, developing an higher velocity if compared to the freestream one.
Considering, specifically, the numerical values of the present simulation, a MFCR=1.65 has been obtained, since the capture area has grown from 0.146 m^2 for the transonic freestream Mach number of 0.85, to 0.409 m^2 for the totally subsonic freestream, meanwhile the highlight section clearly has not been subjected to any variation.
From the considerations made in the introductive chapter of the present work about Mach number evolution, it is easy to see, how at subsonic speeds, a decreasing section leads to an increasing Mach number (Equation 1.18).
The ratio between the Mach number at highlight section and the freestream Mach number is $M_i/M_\infty = 2.33$, with an increment of $\Delta M = 0.2673$, because at highlight $M_i = 0.4684$.
Moreover, an additional flow acceleration takes place along the inlet until the fan face, in which the average Mach number reaches the value of 1.1.
In Figure 3.11 Mach number contours are plotted. In this image the stagnation point position is visible, and, as it was predictable, in this case there is no appearance of a sonic point at the outer nacelle's surface because of the subsonic nature of the incoming flow.

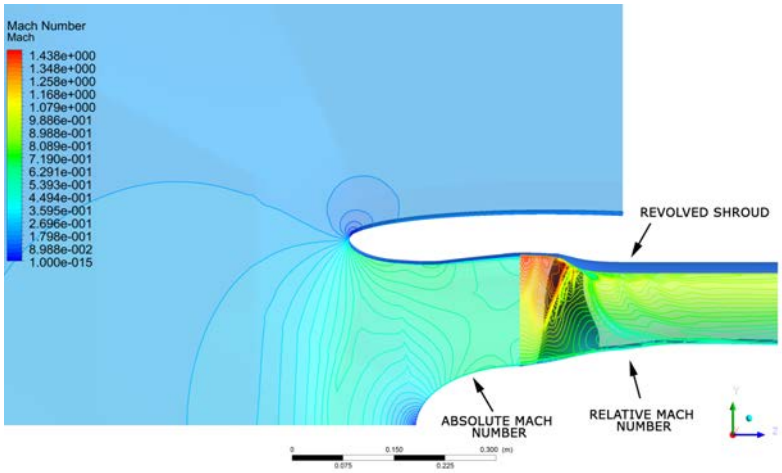

Figure 3.11: *Second case study Mach contours. The blue surface located over the blade and the outlet block represents a portion of the shroud which has been rovolved around propulsor's axis.*

Even though the nature of the airflow upstream the fan blade is completely different, from Figure 3.5 and Figure 3.11's comparison, one can declare that, from the fan face section onwards, the flow mantains the same trend and characteristics.

The previous assertion can be proved also by observing the flow over some blade sections: 30%, 70% and 90% of span from the hub.

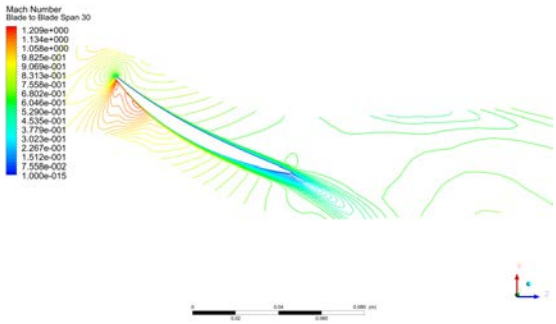

(a) *Relative Mach number at 30% span.*

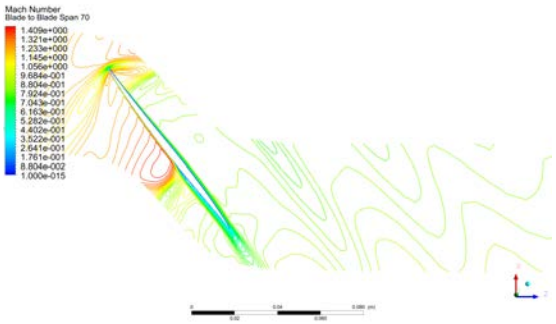

(b) *Relative Mach number at 70% span.*

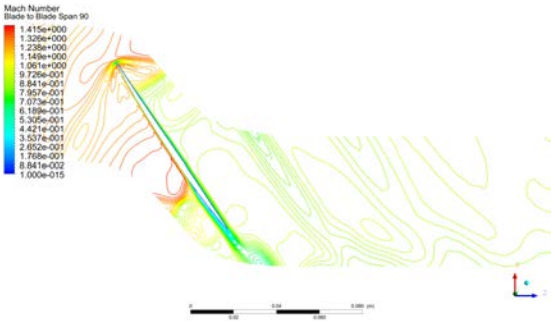

(c) *Relative Mach number at 90% span.*

Figure 3.12: *Blade to blade contours of relative Mach number in the case of* $M_\infty = 0.2$.

Comparing the flow over the blade at the same rotor operating condition at a different inlet configuration ($M_\infty = 0.85$ and $M_\infty = 0.2$) there are no evident discrepancies, leading to the conclusion that the variation of the freestream Mach number doesn't affect flow evolution from the blade onwards.

3.4.1 Intake's Efficiency

As discusses earlier in the present chapter, the inlet's efficiency is influenced by the flight Mach number and the theoretical studies state that both isentropic efficiency (Equation 3.2) and stagnation pressure ratio (Equation 3.1) tend to decrease as the flight speed (i. e. flight Mach number) increases.
In the same way as done for the first case study, intake's performances of the second simulation are analysed and then presented in Table 3.7:

	$M_\infty = 0.85$	$M_\infty = 0.2$
η_D	0.992	0.936
π_D	0.9966	0.998

Table 3.7: *Intake's performances' comparison.*

The total pressure loss, from transonic to subsonic speed, follows the expectations because, however the almost negligible difference, it tends to increase. Focusing on the isentropic diffusion efficiency, the same thing can't be said because it resulted in an opposite trend: as the flight Mach number increases, η_D has increased as a consequence.
Theoretical intake's performances are plotted in Figure 3.13:

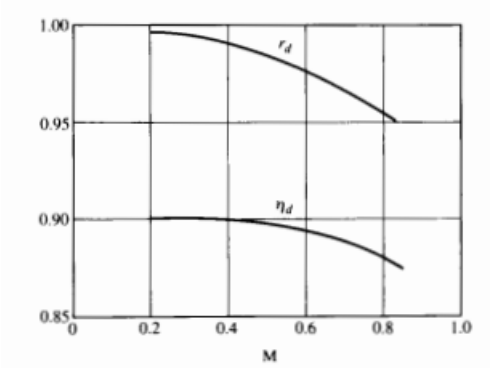

Figure 3.13: *Typical intake's performance, k=1.4 [17].*

Previous η_D's plot is obtained from the following equation, in which Equation 3.2 and Equation 3.1 are combined:

$$\eta_D = \frac{(p^0_{FF}/p_{amb})^{(k-1)/k} - 1}{[(k-1)/2]M^2_\infty} \tag{3.3}$$

The reason behind these obtained unconsistent values about isentropic diffusion efficiency, could be supposed to reside in the fact that Figure 3.13 is based on an analytical relationship which may not take into consideration realistic flight conditions. In other words, the main criterion at the base of the isentropic efficiency definition is represented by the overall fluid's deceleration, which depends on the mass flow rate as well as the Mach number rather than on internal deceleration [17]. Moreover, Figure 3.13, shows typical values of π_D and, since η_D trend was calculated from it, a variance from typical total pressure loss' values, as happens in this CFD model's results, may cause considerable variations on the trend of isentropic diffusion efficiency.

Conclusions

A CFD study has been caried out to simulate the mutual interaction between the three elements which are part of the initial portion of a turbofan engine: intake, fan and spinner. The intake and the nacelle were extracted from the Nasa Common Research Model, the transonic fan is the Nasa rotor 67 also derived from Nasa, finally the spinner has been realised by means of Solidworks, following appropriate geometrical criteria.
The first step consists on the single blade's validation through the comparison of the experimental data with the results obtained from CFD analysis. At this point, the work continues with the most challenging and thorny part, represented by the three components' assembly in order to generate the grid of the entire model.
For both analysis, only a single channel was simulated by ANSYS CFX solver, which solves RANS equations adopting the $k - \omega - SST$ turbulence model and in both cases convergence was reached after a huge amount of iterations by manually changing the maximum timescale until a maximum value of 10^{-4} s.
Since the aim of this work is to create a model able to reproduce realistic situations varying the freestream conditions, one has focused mainly on streamtube shapes entering the propulsor, on intake's performances and on the comparison between characteristic compressor maps of the single blade with the installed one.
Obtained results demonstrated congruence with the expectations, in particular, the first case study, which considers a transonic freestream Mach number of 0.85, presents a divergent streamtube's shape, obtaining a MFCR<1 and a consequently flow's deceleration from $M_\infty = 0.85$ in the farfield, to M=0.47 close to the engine's inlet section. Moreover, it has noticed how the intake causes a little total pressure's loss with a resulting decrease of rotor's isentropic efficiency.
The second case, with a $M_\infty = 0.2$, also denotes the same pre-entry fluid's characteristics of a traditional totally subsonic flow, in which the streamtube has, as it is expected, a convergent shape with a MFCR>1 and an increase in Mach number just before the highlight section.

Even though the previous data underline the correct installation and model construction, a certain discrepancy between the obtained CFD results and the theoretical ones about intake's performances is notable. From simulations, both isentropic diffusion efficiency and total pressure loss result very different with regards to the trends illustrated in Figure 3.13. The supposed reasons concerning this divergence have been already treated in chapter 3.

Future Works

This thesis has been declared to represent a starting point for future analysis which will enlarge the studies about new techniques concerning aeronautical civil engines performances' optimisations.
First of all, a deeper CFD study may be carried out in order to assess all forementioned drag components, so as to provide a rough drag coefficien's estimate. However, to correctly simulate all different flight phases, it is necessary to consider a full annulus model, which could also take into account the actual inlet flow's asymmetry due to incidence angle and to the nacelle highlight section's design angle.
In addition, once correctly assessed c_D value, it would be interesting to proceed with the inlet's shortening until L/D=0.25, and then simulating different flight conditions, such as cruise and take-off. With this procedure, one is able to analyse the effects of shorter nacelles on drag coefficient, in fact it has been proved that the above solution provides an improvement of such parameter.

Bibliography

[1] E. Benini. Propulsione Aerea. *Cleup*, 2005.

[2] M. Robinson, D. G. MacManus, C. Sheaf. Aspects of Aero-Engine Nacelle Drag. *Journal of Aerospace Engineering*, 2018.

[3] T. P. Stankowski, D. G. MacManus, C. T. Sheaf, N. Grech. Aerodynamics of Aero-engine Installation. *SCITECH Forum, 54th AIAA Aerospace Sciences Meeting*, 2016.

[4] A. Peters, Z. S. Spakovszky, W. K. Lord, B. Rose. Ultra-Short Nacelles for Low Fan Pressure Ratio Propulsors. *Proceedings of ASME Turbo Expo 2014: Turbine Technical Conference and Exposition*, 2014.

[5] E. Benini. Dispense del corso di Macchine a Fluido.

[6] A. J. Strazisar, J. R. Wood, M. D. Hathaway, K. L. Suder. Laser Anemometer Measurements in a Transonic Axial-Flow Fan Rotor. *NASA Technical Paper*, 1989.

[7] G. Venturelli. Development of Numerical Procedures for Turbomachinery Optimization. *Università degli Studi di Padova, Tesi di Dottorato di Ricerca in Ingegneria Industriale*, 2015.

[8] E. Benini, R. Biollo. Recent Advances in Transonic Axial Compressor Aerodynamics. *Progress in Aerospace Science*, 2012.

[9] J. C. Vassberg, M. A. DeHaan, S. M. Rivers, R. A. Wahls. Development of a Common Research Model for Applied CFD Validation Studies. 2008.

[10] H. Hoeisel. Aerodynamic Aspects of Engine-Aircraft Integration of Transport Aircraft. *Aerospace Science and Technology, vol.7*, 1997.

[11] L. G. Trapp, H. G. Argentieri. Evaluation of Nacelle Drag using Computational Fluid Dynamics. 2010.

[12] J. Roskam, C. Lan. Airplane Aerodynamics and Performance. *DAR Corporation, Lawrence Kansas*, 1997.

[13] J. D. Anderson Jr. Fundamentals of Aerodynamics. *McGraw-Hill Education*, 2010.

[14] F. Tejero, M. Robinson, D. G. MacManus, C. Sheaf. Multi-Objective Optimisation of Short Nacelles for High Bypass Ratio Engines. *Aerospace Science and Technology*, 2019.

[15] C. D. Harris. NASA Supercritical Airfoils. *NASA TP-2969*, 1990.

[16] A. Cavallini, S. Mancin, M. Sovrano, L. Rossetto. Elementi di Gasdinamica. *Edizioni Progetto Padova*, 2012.

[17] P. Hill, C. Peterson. Mechanics and Thermodynamics of Propulsion. *Pearson Education*, 2014.

[18] W. J. Calvert, R. B. Ginder. Transonic Fan and Compressor Design. *Propulsion Department, DERA Pyestock, Farnborough, UK*, 2015.

[19] G. Abate. Aerodynamic Optimization of a Transonic Axial Compressor Rotor. *Università degli Studi di Padova, Tesi Magistrale in Ingegneria Aerospaziale*, 2012.

[20] M. Tridente. CFD Study in the Effect of a Transonic Fan Downstream of an S-Shape Duct. *Università degli Studi di Padova, Tesi Magistrale in Ingegneria Aerospaziale*, 2019.

[21] Solidworks. Solidworks User Manual. 2018.

[22] Mathworks. MATLAB User Guide. *V. R2018b*, 2017.

[23] Pointwise. Pointwise Y+ Calculator. *https://www.pointwise.com/yplus/*.

[24] D. J. Hill. Compressor Performance Scaling in the Presence of Non-Uniform Flow. *Electronic Theses and Dissertations, 5985*, 2017.

[25] A. Petrusson. Aerodynamic Evaluation of Nacelles for Engines with Ultra High Bypass Ratio. *Chalmers University of Technology, Master's thesis in Applied Mechanics*, 2017.

[26] G. Laurelle. Air Intakes: Role, Constraints and Design. *ICAS Congress*, 2002.

[27] J. Chen, Z. Wang, Y. Wu, A. Wang. Nacelle, Air Intake Aerodynamic Design and Inlet Compatibility. *Gas Turbine India Conference*, 2014.

Ringraziamenti

Chi mi conosce sa che non sono brava a parole ad esprimere tutto ciò che ho dentro, la gratitudine, la stima e l'affetto che provo nei vostri confronti, ma con queste righe voglio almeno provarci.
Questa tesi racchiude tutti i sacrifici a cui questo percorso di studi mi ha portata, dandomi però moltissime gioie, mi ha spinta a superare i miei limiti e ad accettarli qualora non sia stato possibile sormontarli. Non so bene quali parole siano le più adatte, perciò vi dico semplicemente grazie.

In primis ringrazio il prof. Ernesto Benini, la persona che ha reso possibile la realizzazione di questo lavoro, per la disponibilità e la conoscenza che mi ha trasmesso.
Ringrazio Andrea Magrini per avermi seguita durante questi mesi e per il suo fondamentale aiuto.

Grazie alla mia famiglia, a mia madre in particolar modo per avermi supportata e sopportata, dandomi conforto nei momenti peggiori e credendo in me quando nemmeno io avrei avuto la forza per farlo.
Ringrazio Andrea, la mia spalla, per la tua costante presenza nella mia vita, nonché per la tua infinita pazienza. A parole mi risulta estremamente difficile esprimere la mia gratitudine, il mio affetto incondizionato e l'enorme stima che ho nei tuoi confronti, per la persona che sei e per come in questi anni hai saputo prendermi e volermi bene.
Ringrazio Silvia, per tutte le risate in tutti quegli anni dentro e fuori quel campo da pallavolo, per i giri in motorino, per gli spritzetti e i caffè a casa mia.
Un enorme grazie va anche a tutte quelle persone che in questi anni hanno vissuto con me il percorso universitario. Grazie ad Andrea per tutto l'aiuto che mi hai dato durante lo studio e per l'amicizia che ci lega ormai da qualche anno, per la spontaneità e la pazienza.
Grazie alla Sofi, che sebbene ci conosciamo da poco, hai saputo darmi tanto, hai saputo farmi credere in me stessa nei momenti peggiori, grazie di cuore, ti voglio bene.
Ringrazio i "compagni magistrali", per avermi allietato questi anni di specialistica rendendo più leggero questo percorso, in particolar modo Pippo, che senza di lui la mesh sarebbe ancora da ultimare.
Ringrazio infine tutti gli amici con cui, in questi anni, ho condiviso momenti di gioia e divertimento, grazie a tutti!